



HAL
open science

Multiplexed chromatin imaging reveals predominantly pairwise long-range coordination between *Drosophila* Polycomb genes

Julian Gurgo, Jean-Charles Walter, Jean-Bernard Fiche, Christophe Houbron, Marie Schaeffer, Giacomo Cavalli, Frédéric Bantignies, Marcelo Nollmann

► **To cite this version:**

Julian Gurgo, Jean-Charles Walter, Jean-Bernard Fiche, Christophe Houbron, Marie Schaeffer, et al.. Multiplexed chromatin imaging reveals predominantly pairwise long-range coordination between *Drosophila* Polycomb genes. *Cell Reports*, 2024, 43 (5), pp.114167. 10.1016/j.celrep.2024.114167 . hal-04762608

HAL Id: hal-04762608

<https://hal.umontpellier.fr/hal-04762608v1>

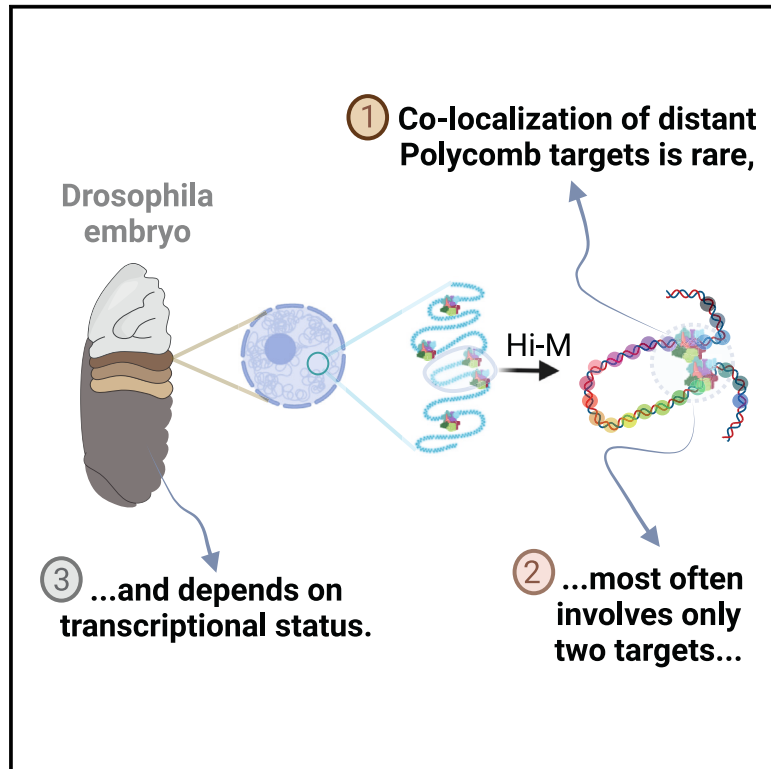
Submitted on 31 Oct 2024

HAL is a multi-disciplinary open access archive for the deposit and dissemination of scientific research documents, whether they are published or not. The documents may come from teaching and research institutions in France or abroad, or from public or private research centers.

L'archive ouverte pluridisciplinaire **HAL**, est destinée au dépôt et à la diffusion de documents scientifiques de niveau recherche, publiés ou non, émanant des établissements d'enseignement et de recherche français ou étrangers, des laboratoires publics ou privés.

Multiplexed chromatin imaging reveals predominantly pairwise long-range coordination between *Drosophila* Polycomb genes

Graphical abstract



Authors

Julian Gurgo, Jean-Charles Walter, Jean-Bernard Fiche, ..., Giacomo Cavalli, Frédéric Bantignies, Marcelo Nollmann

Correspondence

frederic.bantignies@igh.cnrs.fr (F.B.), marcelo.nollmann@cbs.cnrs.fr (M.N.)

In brief

Gurgo et al. explore how Polycomb proteins, crucial for cell identity and development, interact in 3D space. The findings reveal that these interactions are rare, specific, and regulated during development. This enhances our understanding of gene regulation, potentially impacting fields like developmental biology and disease research.

Highlights

- 3D proximity between Polycomb targets is rare in *Drosophila* embryos
- Clustering of Pc genes involves in most cases only two targets
- 3D proximity of Pc targets depends on segment-specific expression



Article

Multiplexed chromatin imaging reveals predominantly pairwise long-range coordination between *Drosophila* Polycomb genes

Julian Gurgo,¹ Jean-Charles Walter,³ Jean-Bernard Fiche,¹ Christophe Houbron,¹ Marie Schaeffer,¹ Giacomo Cavalli,² Frédéric Bantignies,^{2,*} and Marcelo Nollmann^{1,4,*}

¹Centre de Biochimie Structurale, CNRS UMR 5048, INSERM U1054, Université de Montpellier, 60 rue de Navacelles, 34090 Montpellier, France

²Institut de Génétique Humaine, CNRS UMR 9002, Université de Montpellier, 141 rue de la Cardonille, 34396 Montpellier, France

³Laboratoire Charles Coulomb (L2C), Université de Montpellier, CNRS, Montpellier, France

⁴Lead contact

*Correspondence: frederic.bantignies@igh.cnrs.fr (F.B.), marcelo.nollmann@cbs.cnrs.fr (M.N.)

<https://doi.org/10.1016/j.celrep.2024.114167>

SUMMARY

Polycomb (Pc) group proteins are transcriptional regulators with key roles in development, cell identity, and differentiation. Pc-bound chromatin regions form repressive domains that interact in 3D to assemble repressive nuclear compartments. Here, we use multiplexed chromatin imaging to investigate whether Pc compartments involve the clustering of multiple Pc domains during *Drosophila* development. Notably, 3D proximity between Pc targets is rare and involves predominantly pairwise interactions. These 3D proximities are particularly enhanced in segments where Pc genes are co-repressed. In addition, segment-specific expression of *Hox* Pc targets leads to their spatial segregation from Pc-repressed genes. Finally, non-*Hox* Pc targets are more proximal in regions where they are co-expressed. These results indicate that long-range Pc interactions are temporally and spatially regulated during differentiation and development but do not induce frequent clustering of multiple distant Pc genes.

INTRODUCTION

Chromatin is organized in a multi-scale manner, ranging from nucleosomes to chromosomes. At intermediate levels, chromatin is organized in topologically associating domains (TADs), which are regions of DNA that interact more frequently with themselves than with other regions.^{1–5} TADs are thought to play a key role in regulating gene expression.^{6,7} In *Drosophila melanogaster*, TADs are generally smaller than in mammals (~100 kb versus ~800 kb, respectively) and tend to correlate with active and repressed chromatin marks.^{4,8} For this reason, *Drosophila* TADs are classified according to their epigenetic state (i.e., histone post-translational modifications) into active (associated with histone H3 lysine 4 trimethylation [H3K4me3] and histone H3 lysine 36 trimethylation [H3K36me3]), heterochromatic (enriched in histone H3 lysine 9 dimethylation [H3K9me2]), HP1, and Su(var)), black (devoid of specific histone marks), and Polycomb (Pc) repressed, enriched in histone H3 lysine 27 trimethylation (H3K27me3), and bound by Pc group (PcG) proteins.

PcG proteins are conserved in most eukaryotic organisms. They mediate gene repression and are classified into two main complexes, PRC1 and PRC2. In *Drosophila*, PcG proteins are recruited to specific sequences called Polycomb (Pc) response elements (PREs)⁹ by a two-step process¹⁰ involving the deposition of H3K27me3 marks by PRC2, followed by chromatin compac-

tion by PRC1,^{11,12} a complex that contains the chromodomain protein Pc and Polyhomeotic (PH). PcG target genes are often contained within discrete Pc TADs,⁴ which are characterized by a high degree of compaction and intermixing.^{13,14} In single cells, Pc TADs form discrete nano-compartments¹⁵ displaying a cell-type-specific internal organization that responds to the transcriptional state of its PcG genes.¹⁶ Interestingly, PcG proteins form discrete compartments (foci) in the nucleus, both in flies and mammals.^{17–19} Within these Pc compartments, genomically distant PcG target genes can physically colocalize when co-repressed.^{19,20}

In *Drosophila*, Pc TADs tend to be spatially segregated from active domains,^{15,16} consistent with the formation of active and repressive compartments⁴ and with the spatial separation of active and repressive marks in single cells.^{15,21} Taken together, this evidence suggests the possibility that multiple Pc TADs might often associate with each other in single cells to form Pc compartments to reinforce gene repression.

Here, we tested this hypothesis by applying a high-throughput, high-resolution, high-coverage, microscopy-based technology (Hi-M), a method that enables the capture of chromatin conformations in single cells while preserving the spatial information within the specimen.^{22,23} We found that the spatial colocalization of distant PcG genes was rare and in most cases involved only two Pc domains. Formation of hubs involving more



than two Pc domains was highly infrequent. Interestingly, the interaction frequencies between Pc domains were enhanced in regions of the embryo where PcG target genes were co-repressed or co-expressed, indicating that the rare 3D encounters between Pc domains may play a role in reinforcing repression and in co-transcriptional activation.

RESULTS

Chromosome-wide, simultaneous visualization of multiple Pc targets in single cells

To investigate the chromosome-wide organization of Pc target genes, we focused on an ~15-Mb region of chromosome 3R (chr3R) displaying most long-range Pc contacts.^{4,19,24–27} Within this chromosomal region, we identified 19 Pc genomic loci spanning 20 kb based on three criteria (Figures 1A and S1A; STAR Methods): (1) binding of all PRC1 components (PC, polyhomeotic [PH], and posterior sex combs [PSC]), (2) presence of H3K27me3 marks but not of H3K4me3 and H3K36me3 marks, and (3) formation of long-range Pc interactions.²⁸ These 19 Pc regions recapitulated most long-range Pc interactions in this chromosome (>80%; Figure S1B; STAR Methods)²⁸ and included PcG targets within the three large Pc TADs containing *Drosophila*'s *hox* genes: Bithorax (BX-C), Antennapedia (ANT-C), and NK-C, in addition to 8 smaller non-*hox* PcG-regulated target loci (Figure 1A). Next, we used Hi-M, an imaging-based technology that retrieves chromatin architecture in single cells while maintaining spatial context.^{22,23} Hi-M relies on the sequential imaging of tens of distinct genomic loci labeled by Oligopaint-fluorescence *in situ* hybridization (FISH)^{29,30} in intact *Drosophila* embryos (Figures 1B, S1C, and S1D).^{22,23} Hi-M is similar to other multiplexed imaging technologies developed concurrently.^{16,31–35} These multiplexed DNA imaging methods, including Hi-M, were previously used in samples with single cell layers (e.g., cultured cells, *Drosophila* embryos before gastrulation, or cryo-sections). Here, we coupled Hi-M to confocal imaging to be able to visualize the 3D localization of multiple Pc target regions in multi-layered stage 15–16 (S15–S16, 12–16 h of development) embryos without cryo-dissection (Figure 1B).

For this, we designed, amplified, and hybridized an Oligopaint-FISH library where each of the 19 Pc loci in chr3R (Figure 1A) was encoded by a single barcode. Barcodes were sequentially imaged as described previously²³ (see STAR Methods and Figures S1E, S1F, and S2A for more details). Next, we calculated the mean pairwise distance and ensemble proximity frequency maps for wild-type S15–S16 embryos from a large number of cells ($N = 22,243$; Figure 1C; STAR Methods). To validate the method, we first compared the Hi-M proximity frequency matrix for S15–S16 embryos (calculated with a proximity threshold of $T = 250$ nm), with the publicly available Hi-C contact matrix for S16 embryos²⁸ (Figure S2B). Both matrices display a similar organization, notably the presence of TADs and long-range interactions. To further test the robustness of the method, we calculated the Pearson correlation between Hi-M proximity frequencies and Hi-C contact frequencies as a function of proximity threshold and genomic distance (Figure S2C). For proximity distance thresholds equal to or higher than 250 nm, Hi-M and

Hi-C data displayed similar levels of correlation; thus, we chose a proximity threshold of 250 nm to calculate proximity frequencies. To further validate this choice, we calculated the Pearson correlation coefficient between Hi-M matrices obtained with different proximity thresholds (between 100 and 400 nm). In all cases, the correlation of Hi-M matrices obtained with different thresholds and between replicates was high ($p > 0.9$) (Figures S2D and S2E).

Barcodes within large Pc TADs (ANT-C, BX-C, and NK-C) displayed high-proximity frequencies and short pairwise distances (PWDs) (Figure 1C), consistent with previous observations in *Hox* TADs^{4,16,20,36} (Figure 1C, black boxes). In addition, we also observed that BX-C and ANT-C, two distant *Hox* TADs, displayed preferential proximities (Figure 1C, green arrows), as expected from previous Hi-C and microscopy reports.^{4,19} Interestingly, long-range proximities between other PcG targets were inhomogeneous, indicating that not all PcG targets have the same probability to interact with each other.

As an additional control, we analyzed the proximity frequencies between Pc, active, and black chromatin regions. For this, we designed an Oligopaint library encompassing ~2 Mbp of chr3R containing intersped Pc, active, and black chromatin regions (Figure S2F). We performed Hi-M experiments on S15–S16 wild-type embryos with this second Oligopaint library and calculated the observed/expected proximity map (Figure S2G; STAR Methods). We observed higher normalized proximity frequencies for black-black, active-active, or Pc-Pc barcodes, as expected (Figures S2G–S2I).

Long-range contacts between Pc targets are known to rely on PcG proteins.¹⁹ Thus, we expected 3D proximity to decrease in embryos lacking essential components of the PcG machinery. We tested this hypothesis by performing Hi-M in homozygous Pc mutant embryos. These embryos showed a loss of 3D proximity both at short-range (within *hox* TADs; Figure 1D, yellow arrows) and at long ranges (e.g., between distant Pc barcodes; Figures 1D, green arrow, and S2J; $p = 4.10^{-5}$). Overall, these results indicate that 3D proximity between Pc barcodes is diminished in the absence of PcG components.

Next, we reasoned that long-range 3D proximity between Pc barcodes should be reduced before the establishment of Pc repression programs during development. To test this, we imaged the organization of Pc barcodes in nuclear cycle 14 (NC14/stage 5) embryos. Interestingly, barcodes within *Hox* TADs were already proximal in this early developmental stage (Figure 1E, black boxes). However, long-range proximities between Pc barcodes were drastically depleted (Figure 1E). Nuclei in NC14 embryos displayed larger overall sizes than at stage 15 (~10%); however, these differences were considerably smaller than the overall difference in long-range distances between these two stages (~50%). Overall, these results suggest that the local organization of Pc targets into TADs precedes the establishment of 3D long-range Pc contacts.

Proximity frequencies between distant Pc targets are described by an equilibrium globule

To shed light onto the mechanisms responsible for the chromosome-wide organization of PcG targets observed by Hi-M, we resorted to a modeling approach that implements a lattice block

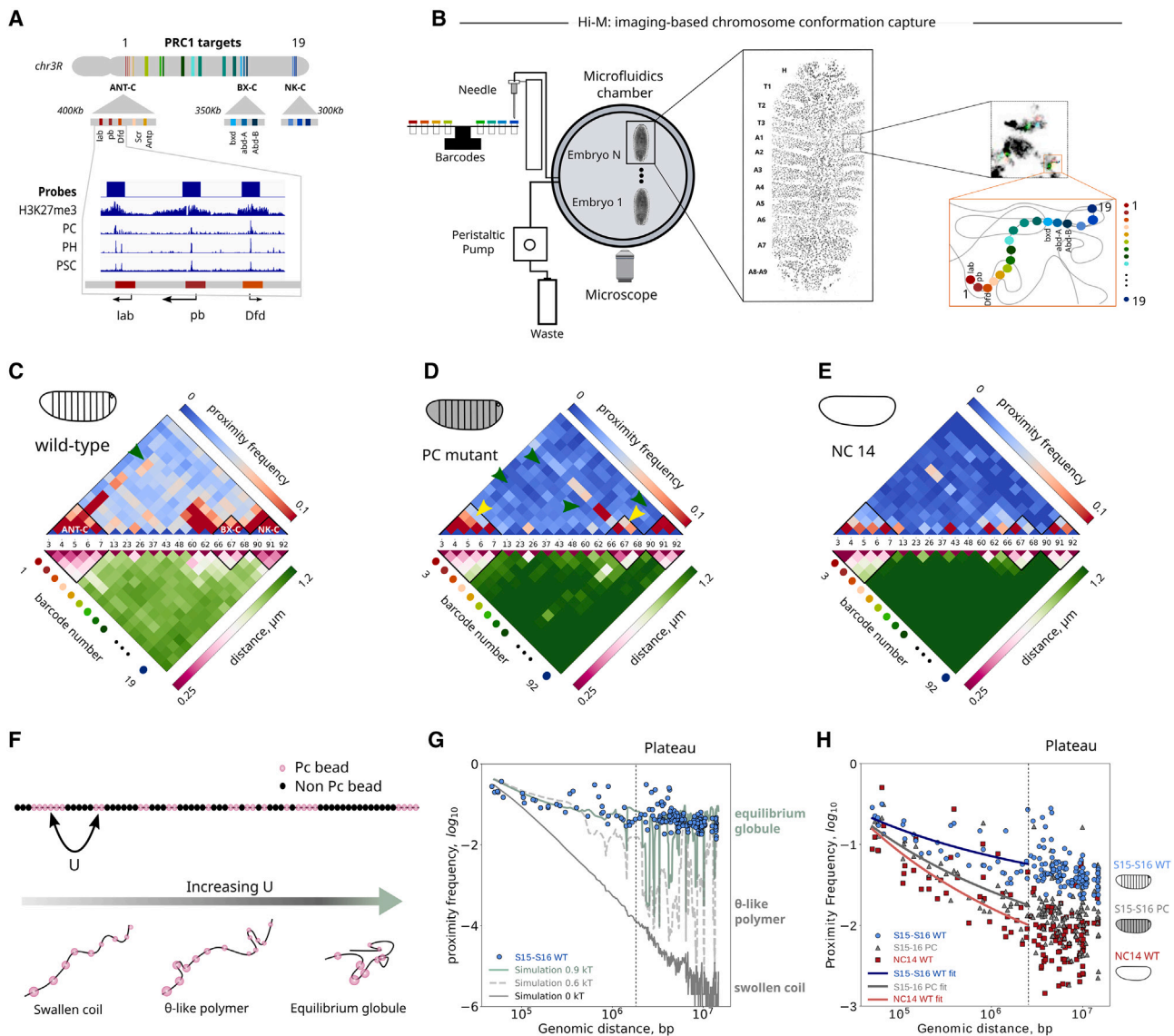


Figure 1. Long-range proximities between distant Pc domains are best described by a self-interacting polymer in the globule regime

(A) Schematic of the Oligopaint library used, covering Pc domains over a portion of ~ 12 Mb of chr3R. Triangles represent the three larger domains: ANTP-C, BX-C, and NK-C. Bottom: H3K27me3, PC, PH, and PSC chromatin immunoprecipitation (ChIP-seq) data for a region of the ANTP-C domain.

(B) Diagram of the experimental setup. Hi-M allows imaging Pc domains sequentially in single cells of full embryos, keeping spatial resolution. Briefly, images are acquired using an Airyscan confocal microscope coupled to a fluidics system. Barcodes are injected using a needle attached to a translation stage. A peristaltic pump delivers solutions into the microfluidics chamber. See supplemental information for a detailed description of the setup.

(C–E) Hi-M proximity frequency maps (top) and pairwise median distance maps (bottom) for S15–S16 embryos (C; $N = 22,243$, $n = 20$, 5 replicates), Pc mutant (D; $N = 26,466$, $n = 16$, 2 replicates), and NC14 WT embryos (E; $N = 13,300$, $n = 17$, 2 replicates). Barcode identities are indicated on the axis. Colormaps corresponding to the proximity frequency and PWD are shown above and below the maps, respectively. Proximity frequency maps were calculated with a distance threshold of 250 nm. Black squares highlight the three larger Pc domains in chr3R (ANTP-C, BX-C, and NK-C).

(F) Polymer modeling of chr3R. Shown is a co-polymer containing interacting beads with energy U (Pc beads, pink), and non-interacting beads (black). Increasing U leads to three different behaviors: swollen (random) coil, θ -like polymer, and equilibrium globule.

(G) Proximity frequency vs. genomic distance for WT S15–S16 embryos (blue circles), and for simulations of a self-interacting polymer in the globule regime (green curve, $U = 0.9 k_B T$), a polymer at the θ -like transition (gray dashed curve, $U = 0.65 k_B T$) and of a polymer in the swollen coil regime (solid gray curve, $U = 0 k_B T$).

(H) Proximity frequency vs. genomic distance, for WT S15–S16 embryos (blue circles), Pc mutant embryos (gray triangles), and NC14 embryos (red squares). Solid lines represent power-law fits to the experimental data with an exponent of $3/2$. A plateau in proximity frequency can be observed at genomic distances higher than ~ 1 Mb.

copolymer model (Figure 1F; STAR Methods).³⁷ In short, the chromosome was modeled by 866 beads with two possible identities: Pc or not Pc. The size of the beads in the simulation (20 kb) was slightly larger than the genomic size of Pc barcodes in our experiments (15 kb). The genomic distribution of Pc beads mirrored the location of PcG targets in chr3R used in Hi-M experiments (Figure 1A), with all intervening beads labeled as non-Pc, as suggested by previous modeling studies.³⁷ The phase diagram was established by calculating two estimators as a function of the interaction strength between Pc monomers (U): the internal energy E , characterizing the average number of contacts between two Pc beads, and the squared radius of gyration (R_g^2), characterizing the spatial extension of the polymer (mean square distance of the monomers with respect to the center of mass; STAR Methods).

The polymer displays three different regimes: swollen coil ($U < 0.65$ k_BT), θ -like polymer ($U \sim 0.65$ k_BT), and equilibrium globule ($U > 0.65$ k_BT) (Figures 1F, S2K, and S2L).^{1,37,38} In the swollen coil regime, the proximity frequency $P(s)$ between monomers separated by a genomic distance s scales as $P(s) \sim s^{-3\nu}$, where $\nu \sim 0.588$ is the Flory exponent of a (non-interacting) self-avoiding polymer (Figure 1G, gray solid curve). In the globule regime, beads attract each other, and the proximity frequency between monomers scales as $P(s) \sim s^{-3/2}$ before reaching a plateau at genomic distances corresponding to the boundary of the globule (Figure 1G, green curve). At the so-called θ -point, the fluctuations in E and R_g display a maximum (at the critical energy $U_c \sim 0.65$ k_BT for our model) (Figures S2K and S2L; STAR Methods) where attractive interactions between beads compensate exactly for the swelling due to self-avoidance, leading to Gaussian statistics with the proximity frequency between monomers scaling as $P(s) \sim s^{-3/2}$ at all scales (Figure 1G, gray dashed curve). In our particular case, the θ -like transition has to be considered with caution due to the inhomogeneous distribution of Pc beads; high-density regions of Pc beads are already in the (equilibrium) globule regime, while regions of low Pc bead densities are still in the swollen coil regime (see the inhomogeneities of the proximity frequency in Figure 1G for the θ -like polymer).

To determine the regime that best describes the 3D folding of PcG targets in chr3R, we plotted the experimental proximity frequency as a function of genomic distance $P(s)$. The experimental data for S15–S16 wild-type (WT) embryos was best represented by an equilibrium globule ($U = 0.9$ k_BT; Figure 1G). Typical conformations obtained from modeling are shown in Figure S2M. Below ~ 1 Mb, the experimental proximity frequency decreases with genomic distance as $s^{-3/2}$; thus, it follows the random-walk statistics (Figure 1H). This behavior is consistent either with the general repulsion of the polymer balancing by nuclear confinement or by attractive forces (e.g., between Pc, black, or active chromatin domains). We favor the latter because of the low volumetric fraction of chromatin in *Drosophila* nuclei ($\sim 0.01\%$). Above ~ 1 Mb, the proximity frequency reaches a plateau, characteristic of block copolymers.³⁹ We note that the energy required to simulate the equilibrium globule that best represents the experimental data is close to the thermal energy (k_BT). At this energy, we do not observe the hallmark of microphase-separated block copoly-

mers; namely, where the two components (e.g., Pc and non-Pc beads) are non-uniformly distributed in space and display regions of local spatial enrichment where distant components concentrate.^{40,41}

We then sought to determine which polymer folding regime best described the experimental $P(s)$ for NC14 embryos. Interestingly, for NC14, the $P(s)$ curve was also best represented by an equilibrium globule but with a lower interaction energy ($U = 0.8$ k_BT). We note that this difference in interaction energy between NC14 versus S15–S16 embryos is small (0.1 k_BT) but can still lead to a large overall energy difference when integrated over the whole chromosome (containing 75 Pc beads), thus considerably impacting the global organization of the chromosome (see below). This reduction in interaction energy between S15–S16 and NC14 WT embryos suggests a role of Pc components in enhancing interactions between distant Pc targets.

To test this prediction, we examined the differences in experimental $P(s)$ curves between S15–S16 WT, Pc mutant, and NC14 embryos. Proximity frequencies were notably reduced in the absence of Pc and declined rapidly in NC14 embryos, consistent with our previous conclusions regarding the role of PcG proteins in mediating long-range interactions between PcG targets (Figure 1H). Surprisingly, $P(s)$ curves for Pc-depleted and NC14 embryos still exhibited a plateau above ~ 1 Mb, characteristic of an equilibrium globule (Figure 1H). Furthermore, the plateau was also present when simulating the whole chr3R (Figures S2N and S2O), with proximity frequencies above ~ 15 Mb being extremely low ($<0.5\%$; Figure S2O). Overall, these results are consistent with PcG proteins reinforcing interactions between Pc targets and suggest that other factors (e.g., HP1, chromatin insulators, active transcription)^{25,42,43} are likely also involved in regulating long-range chromosomal interactions in *Drosophila*.

Chromosome-wide association of Pc targets involves predominantly pairwise interactions

In *Drosophila*, Pc components assemble into large Pc compartments.^{17–19} These results suggest that Pc compartments may involve the spatial clustering of multiple PcG targets. To test this hypothesis, we calculated how often a Pc barcode was proximal (at a distance ≤ 250 nm) to any other Pc barcode in single cells. Targets within large Pc domains (i.e., ANT-C, BX-C, and NK-C) were combined to focus on long-range Pc contacts. In S15–S16 embryos, two or more distant Pc barcodes were found to spatially co-localize in only $3.7\% \pm 1.7\%$ of cells (Figure 2A). This frequency was comparable for all Pc barcodes investigated and was in all cases lower than 10%. As expected, this frequency of co-localization was even lower for NC14 embryos ($1.4\% \pm 1\%$) (Figure 2B), consistent with the loss of long-range Pc proximity in early embryos (Figure 1E), and suggesting that Pc architecture is gradually acquired during development. To determine whether this behavior was dependent on the proximity distance threshold, we calculated the mean colocalization frequency of Pc barcodes for different distance thresholds (Figure 2C). The mean proximity frequencies remained lower than 15% in most cases, even for distance cutoffs as large as 400 nm. For early embryos, the mean proximity frequencies were considerably lower (Figure 2D). As expected, the mean co-localization frequency was positively correlated with the

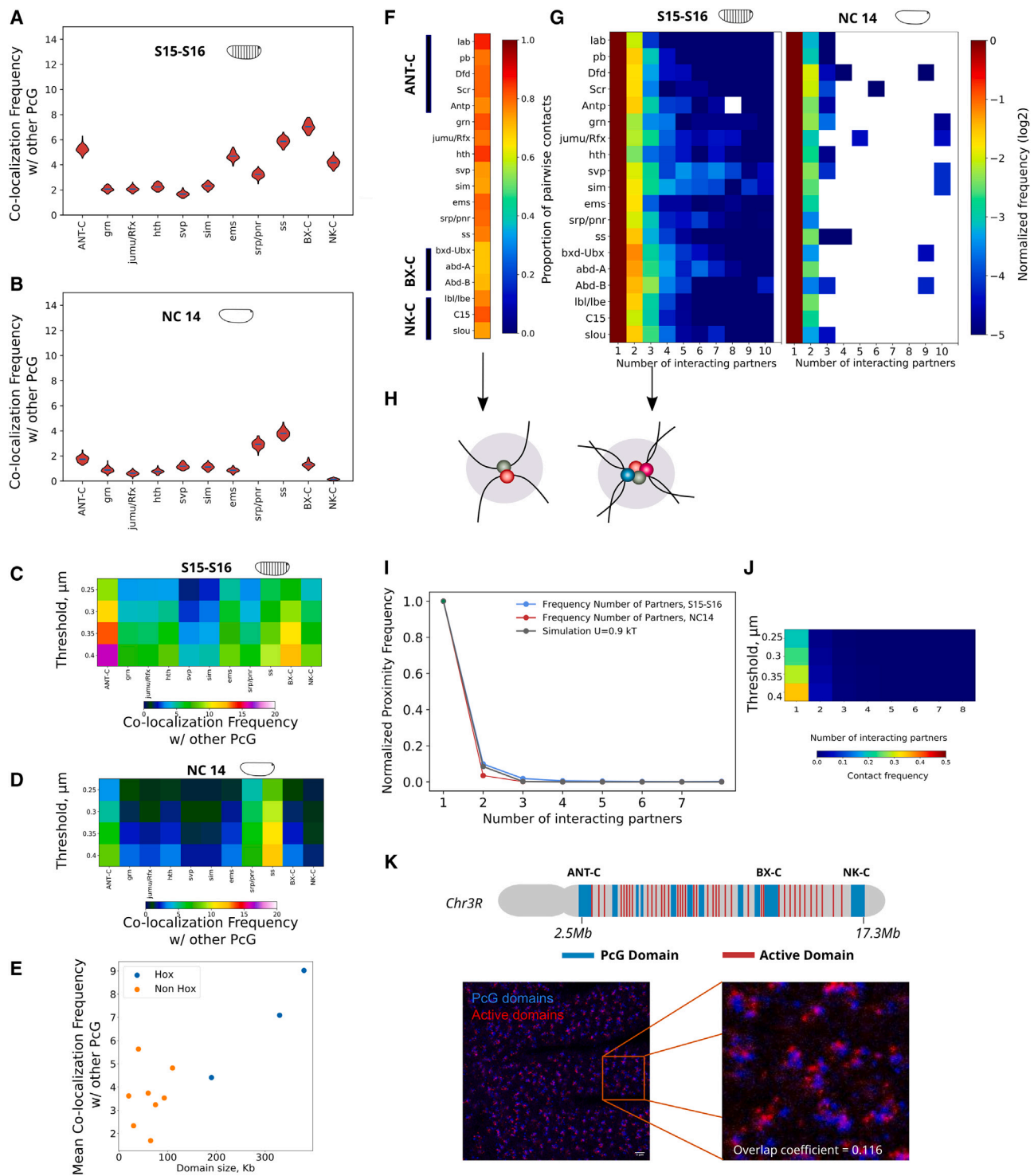


Figure 2. Distant Pc genes rarely co-localize in 3D and predominantly involve only two Pc targets

(A and B) Violin plot distributions representing the frequency with which each Pc domain interacts with any other Pc domain encoded in our Oligopaint library for S15–S16 (A) and NC14 embryos (B) (STAR Methods). A gray line represents the mean. The difference of the mean values between the two developmental stages is statistically significant (independent t test, $p < 0.01$) for all domains. We speculate that the higher co-localization frequencies for *srp/pnr* and *ss* may be linked to their close genomic proximity (390 kb), a distance considerably shorter than for the other Pc barcodes in the figure (>1 Mb). Error bars represent standard error of the mean.

(legend continued on next page)

size of the Pc domain within which the Pc barcode was located (Figure 2E), consistent with a role of PcG components in mediating long-range interactions between Pc domains. Thus, in single cells, during embryogenesis, Pc targets within Pc domains rarely spatially co-localize with other Pc targets to form clusters.

To explore whether these infrequent spatial encounters involved multiple Pc targets, we calculated the proportion of clusters containing two (i.e., pairwise cluster) or more Pc targets (multi-way cluster). Clusters containing only two Pc targets were the most common in all cases (>70%) (Figure 2F). Next, we calculated the frequency of multi-way clusters as a function of the number of targets in a cluster, normalized by the pairwise cluster frequency (Figure 2G). This normalized frequency of multi-way interactions decreased monotonically with the number of co-localizing targets, inconsistent with Pc compartments arising from the nucleation of multiple Pc targets. Notably, this behavior was not tissue specific, as the trend was similar for all segments of the embryo (Figure S3A). For NC14 embryos, Pc clusters almost exclusively contained two targets, with the frequency of multi-way clusters being almost negligible (<5%; Figures S3B and 2G). All in all, these results suggest that Pc targets rarely form clusters, and when they do, the cluster contains a very limited number of targets (Figure 2H). These conclusions are in full agreement with our previous results indicating that distant Pc targets co-localize in 3D infrequently.

To further test these conclusions, we calculated the frequencies with which multiple Pc targets co-localized in the block copolymer model presented above ($U = 0.9 k_B T$) (Figure 1F) and compared them to the experimental frequencies (Figures 2I and 2J). The co-localization frequency between Pc beads in the model was $\sim 10\%$, comparable to our experimental measurements ($\sim 4\%$; Figure 2A). In addition, the relative frequencies of pairwise and multi-way clusters were also comparable between experimental and simulated data (Figure 2I). Thus, our simple polymer model reproduces the low experimental frequencies of pairwise and multi-way proximities, suggesting that the entropy of the polymer dominates over the enthalpic contributions provided by attractive interactions between Pc targets.

To further validate this hypothesis, we devised a toy polymer model containing two Pc targets (one in each end) and characterized its behavior for different Pc interaction energies (U) and

polymer lengths (L) (Figure S3D). We found that the interaction energy required to bring Pc beads together increased logarithmically with polymer length (Figure S3E), while in a first approximation, the entropy barrier to bring the two Pc beads together scales, at leading order, like the log of the chromatin length. Thus, the entropy of chromatin acts to counteract the tendency of Pc targets to coalesce in space, providing a rationale for the infrequent 3D co-localization of Pc targets observed for the full chromosome.

Finally, we designed and imaged an Oligopaint library labeling the 19 Pc targets in chr3R (Figure 1A; shown in blue in Figure 2K) as well as the 39 active regions between them (Figure 2K, red; STAR Methods). In most cells, Pc and active domains were spatially segregated (Figure 2K; overlap coefficient, 0.1; Pearson's correlation coefficient, 0.095). From the genomic distribution of Pc targets in the Oligopaint library, a maximum of 11 Pc domains should be resolvable (Figure S3C). This estimation is lower than the total number of Pc targets in our design (19), as targets in close genomic proximity (i.e., inside ANT-C, BX-C, and NK-C) would appear as single diffraction-limited spots. Considering our efficiency of barcode detection and the probability of pairwise co-localization of two Pc domains, we estimate that we should be able to visualize ~ 7.3 barcode spots per cell (see the legend of Figure 2K and Figure S3F). Remarkably, we observed 7 ± 2 Pc target spots per cell, consistent with a low degree of spatial clustering. All in all, these data and simulations indicate that the spatial coalescence of distant Pc targets is limited.

Gene repression and expression change the 3D internal organization of Pc domains

Our data show that interactions between distant Pc targets are rare and involve primarily two targets. To determine whether these interactions depend on the transcriptional status of the co-localizing Pc targets, we mapped proximity frequencies for different segments of the embryo displaying distinct transcriptional programs. First, we focused on intra-domain interactions within *hox* TADs. These TADs contain the genes responsible for the development of body segments and display well-defined patterns of expression and repression along the antero-posterior axis of the embryo.^{44–47}

(C and D) Map of mean frequency of Pc-Pc interactions (as in A and B) for different proximity thresholds (between 250 nm and 400 nm) for S15–S16 (C) and NC14 embryos (D).

(E) Mean inter-domain proximity frequency as a function of domain size for S15–S16 embryos. Pc domains are separated as *Hox* and non-*Hox*. Distance threshold = 250 nm.

(F) Proportion of pairwise (2 partners) versus multi-way Pc interactions (>2 partners). Pc genes are indicated on the left, and the colorbar represents normalized frequencies.

(G) Histograms of long-range Pc interactions as a function of the number of interacting partners, normalized by the number of pairwise interactions (1 interacting partner), for late S15–S16 (left) and NC14 (right) embryos. Pc genes are indicated on the left, and the colorscale represents normalized frequency in log₂ scale.

(H) Schematic representing Pc clusters with (left) 1 (i.e., pairwise) and (right) 3 partners.

(I) Normalized proximity frequency versus number of interacting partners for WT S15–S16 embryos (blue curve), NC14 embryos (red curve), and simulations of a co-polymer in the equilibrium globule regime ($U = 0.9 k_B T$, gray curve).

(J) Experimental proximity frequency versus number of interacting partners for proximity thresholds between 250 nm and 400 nm (WT S15–S16 embryos).

(K) Multiple active (red) and Pc domains were labeled in chr3R (blue) (top) and then imaged together using conventional two-color confocal microscopy. Pearson's colocalization coefficient (0.095) and overlap coefficient (0.16) were consistent with segregation of active and Pc domains. Estimation of the number of expected Pc target spots: the three *Hox* domains contain several barcodes; thus, they will be detected with a high probability $p = 1 - (1-p_0)^N > 94\%$, considering a detection efficiency of $p_0 = 0.6$ and a number of barcodes of $i = 3$. The remainder will be detected with an efficiency p_0 ; thus, the average number of detectable domains is $\sim 3 + 8 * p_0 = 7.8$. Two Pc domains come in close proximity, and therefore cannot be spatially resolved, at a frequency of ~ 0.06 (Figure S3F). Thus, we expect to detect, on average, $7.8 - 0.06 * 7.8 \sim 7.3$ domains. Scale bar = 5 μ m.

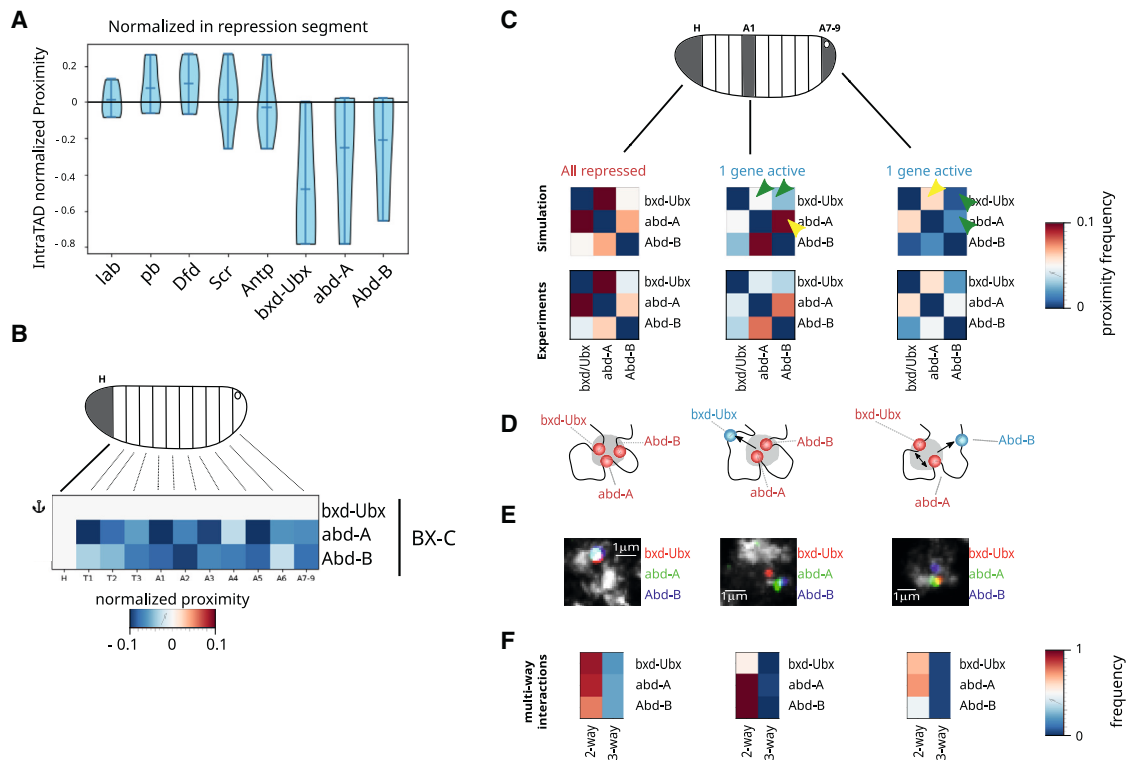


Figure 3. Regulation of gene expression changes chromatin organization within Hox Pc TADs

(A) Violin plots displaying the normalized proximity frequency distributions for each Hox gene within chr3R with respect to the repression segment (A7–A9 for ANT-C, H for BX-C). Only intra-TAD proximities were considered. Normalized proximity frequencies were calculated by subtracting the proximity frequency of the segment minus that of the segment of repression. Violin plots were created by combining the normalized proximity frequencies for all segments for each anchor gene.

(B) Intra-TAD normalized proximity frequency maps for *bxd-Ubx*, normalized in the segment where all Hox genes in BX-C are repressed (head).

(C) Top: diagram showing segments where PcG genes within BX-C are all repressed (head) or where at least one target is active (A1, A7–A9). Middle matrices: simulated and experimental proximity frequency maps for Hox genes within BX-C in the head, A1, and A7–A9. Yellow arrows represent regions displaying higher proximity frequencies and green arrows regions with lower proximity frequencies.

(D) Diagram representing the segment where proximity between Hox genes is highest (head) and segments where the gene being expressed lost proximity to the other Hox genes within the TAD (*bxd-Ubx* in A1 and *Abd-B* in A7–A9).

(E) Representative microscopy images for the three Hox genes within the BX-C domain described in (D). Scale bars = 1 μm .

(F) Intra-TAD frequencies of multi-way proximity for BX-C in the segments highlighted in (D). In all segments, the frequency of pairwise interactions is predominant and diminishes upon gene activation. The frequency of 3-way interactions is the highest for the head, where all genes are repressed.

We exploited the ability of Hi-M to provide spatial distance information to calculate the average proximity frequency of a *hox* target gene within BX-C and ANT-C to all other *hox* genes within their domain. We performed this measurement for each Pc gene (anchor) within BX-C and ANT-C and for each segment of the embryo (Figure 3A). We relied on existing transcriptional data to identify the segment where each gene was repressed (Figure S4A) and used them to normalize the proximity frequencies with respect to the segment of maximum repression for each anchor (segments A7–A9 for ANT-C, head for BX-C). These normalized frequencies were used to detect whether the expression of a Pc target gene changed the frequency with which it co-localized with the other *hox* genes within its TAD (Figure 3A). For BX-C, intra-TAD normalized proximity frequencies were negative, indicating that gene repression consistently led to higher colocalization frequencies for the *hox* genes within BX-C (Figures 3A and 3B). This result is consistent with previous observations.^{20,36}

ANT-C displayed a more complex behavior, with targets exhibiting a small negative change (*Antp*), no overall change (*lab*, *Scr*), or even positive changes (*pb*, *Dfd*) when normalized by their segment of repression (Figures 3A and S5A). Thus, we conclude that repression of *hox* genes does not always lead to the most compact TAD configuration, perhaps due to the existence of more compact TAD conformations in segments where a subset of Pc targets are expressed (see next paragraph).

Next, we tested whether the simple copolymer model proposed above (Figure 1F) was able to qualitatively reproduce these observations. For this, we performed simulations under three scenarios. (1) all three genes within the BX-C domain are repressed (head). In this case, the three genes in BX-C interact with energy U . (2) *bxd-Ubx* is expressed, and *abd-A/Abd-B* are repressed (segment A1). (3) *Abd-B* is expressed, and *bxd-Ubx/abd-A* are repressed (segments A7–A9). In the last two cases, repressed genes interact with energy U , while the region

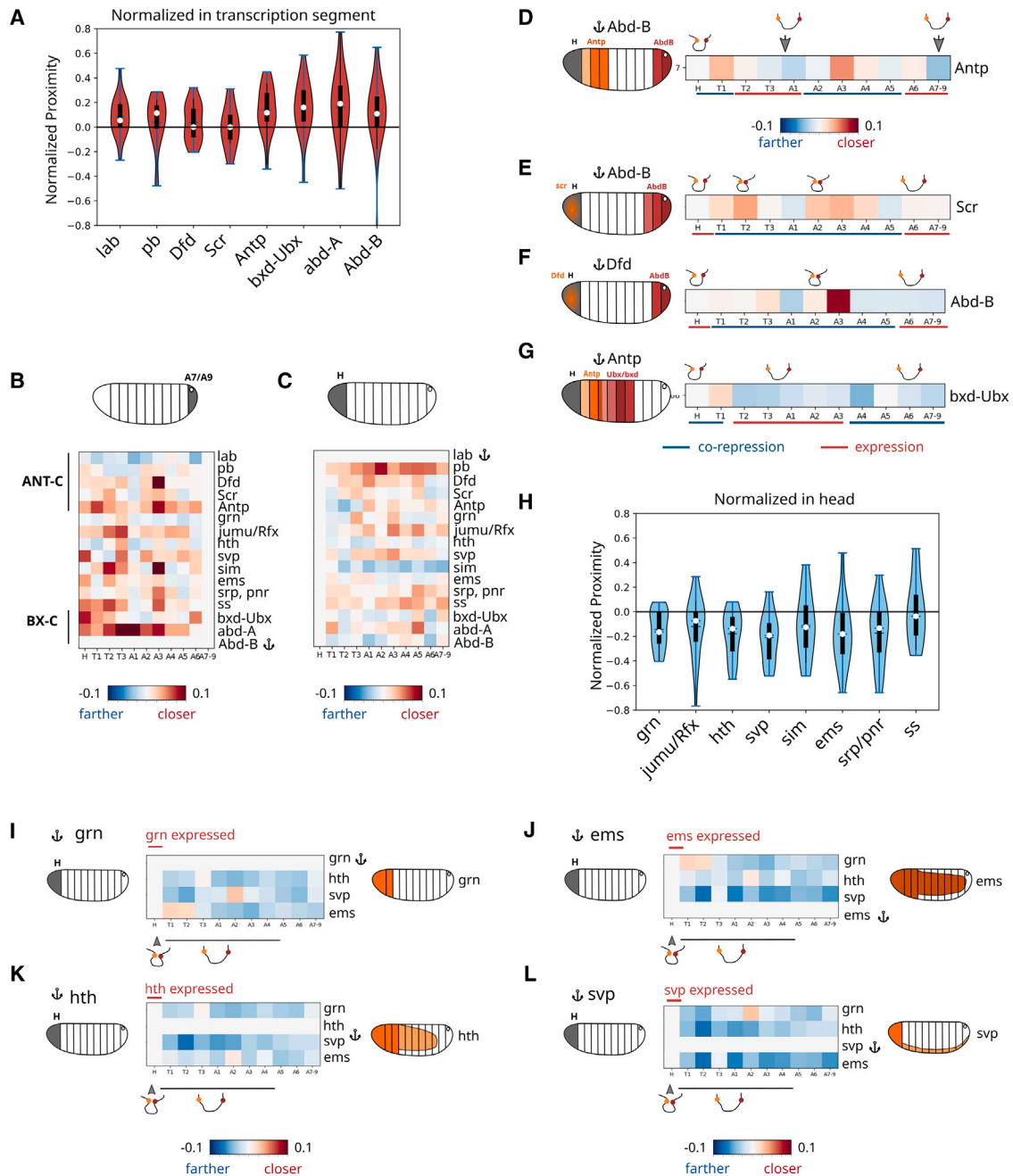


Figure 4. Pairwise, long-range chromatin interactions between Pc domains correlate with expression patterns

(A) Co-expressed and co-activated genes display an increase in physical proximity. Violin plots display the normalized proximity frequency distributions for each Hox gene within chr3R. All Pc barcodes were used in the analysis and thus include intra- and inter-TAD proximities. Normalized proximity frequencies were calculated by subtracting the proximity frequency of the segment minus that of the segment of expression. Violin plots were created by combining the normalized proximity frequencies for all segments for each anchor gene. Error bars represent standard deviations.

(B and C) Normalized proximity frequency maps for different anchors and segments. Anchors were selected at *Abd-B* (left) and *lab* (right). Proximity frequencies were normalized with respect to the segment of expression of the anchor: A7–A9 (left) or head (right).

(D–G) Segment-specific normalized proximity frequency maps for long-range interactions for a selection of anchors (*Abd-B*, *Dfd*, and *Antp*) and targets (*Antp*, *Scr*, *Abd-B*, *bxdl/Ubx*). Proximity frequencies were normalized with respect to the head (gray shade in the schematics). Approximate patterns of expression of anchors and targets are shown in red or orange in the schematics (left). Drawings above the maps represent changes in looping interactions between anchors and targets for different segments. Horizontal lines below the maps highlight the segments where the anchors and targets are co-repressed (blue) or where one of them is expressed (red).

(legend continued on next page)

containing the active gene is considered as non-interacting. To compare results from simulations and experiments, we plotted the proximity frequency matrices for BX-C for the head, segment A1, and segments A7–A9 (Figure 3C). Notably, the simulations were able to reproduce experimental data in the three different segments. In the head, where all genes within BX-C are repressed, proximities between Pc targets were high, notably between *bxd-Ubx* and *abd-A* and *bxd-Ubx* and *Abd-B*. In segments A1/A7–A9, Pc targets in active regions were less often proximal to repressed targets (Figure 3C, green arrows, and 3D and 3E). This phenomenon can also be seen by plotting the proximity frequencies normalized by the segment of expression for each gene in BX-C (Figures S5B). Notably, in these segments, the proximity frequency between repressed genes was enhanced, likely triggered by the loss of interactions with the activated target within the TAD (Figure 3C, yellow arrows, and 3D and 3E). Thus, changing the interactions between Pc target genes in the lattice copolymer model was enough to qualitatively reproduce the trends in the experimental proximity maps.

We previously established that clusters of Pc targets predominantly involved two genes (Figure 2). To determine whether this property depended on cell type or epigenetic state, we analyzed the distribution of multi-way interactions in the head, A1, and A7–A9 segments (Figure 3F). In all segments, the frequency of pairwise interactions was predominant, and diminished upon gene activation, consistent with our previous results. The frequency of 3-way interactions was highest for the head, where all genes are repressed. Overall, these results indicate that formation of higher-order complexes involving multiple Pc targets (more than two) within a TAD is modulated by epigenetic state but remains rare, even in segments where all Pc targets within the TAD are repressed.

Chromosome-wide 3D physical proximity between Pc domains increases in both repressed and co-expressed segments

Next, we investigated whether the co-localization of Pc targets located in different TADs also correlated with their transcriptional state. For this, we calculated the normalized proximity frequency between *Hox* genes and all other Pc targets in chr3R. Proximities were normalized to segments in which the target genes are maximally expressed (Figure S4). For most Pc targets, the normalized proximity frequency displayed positive values (Figures 4A–4C); thus, *Hox* genes co-localized more often with other Pc targets in segments where they were repressed. We note, however, that this was not the case for all Pc target pairs, as indicated by negative proximities in Figures 4A–4C. Overall, these results indicate that activation of *Hox* genes not only leads to their local spatial segregation from other Pc genes within their TAD (Figure 3) but also to less frequent colocalization with more distant Pc targets (Figures 4A–4C and S6A–S6C).

Next, we explored how co-localization frequency changed with the transcriptional status of both anchor and target. For this, we analyzed the changes in proximity maps for different anchors and targets, in all cases normalized by the head, where most of the *Hox* genes are repressed (Figures 4D–4G). We observed that co-localization frequency between two distant Pc targets was highest in segments where both genes were repressed and diminished in segments where one or the other gene was activated (Figures 4D–4G and S6D; Wilcoxon rank-sum test $p = 0.006$). For instance, the proximity between *Abd-B* (anchor) and *Antp* (target) diminished between T2 and A1, where *Antp* is active, and increased in A3–A4, where both targets are repressed (Figure 4D). In the tail (A7–A9), expression of *Abd-B* and other genes within BX-C is correlated with an overall loss of proximity between *Abd-B* and *Antp*. Similarly, *Abd-B* and *Scr/Dfd* displayed the highest proximity frequency in segments where they are both repressed (Figures 4E and 4F). A similar behavior was observed for *Antp* (anchor) and *bxd-Ubx* (target) (Figure 4G). We note exceptions where co-repression did not lead to higher proximity frequencies. For instance, *Antp* and *bxd/Ubx* are repressed in the tail segments; however, their normalized proximity is lower than in the head (Figure 4G), possibly related to the expression of *Abd-B* in the tail segments. Similarly, the colocalization frequency between *Abd-B* and *Scr* (Figure 4E) or *Dfd* and *Abd-B* (Figure 4F) is lower in A1 than in the head, perhaps related to the expression of *Antp* or *Ubx* in this segment. Thus, spatial colocalization between distant *Hox* Pc targets tends to be highest in segments where both targets are repressed and tends to be lower in segments where one of the targets is activated.

Finally, we tested whether non-*Hox* Pc target genes displayed a similar behavior. For this, we calculated the proximity maps for the non-*Hox* targets displaying clear antero-posterior expression patterns: *ems*, *hth*, *svp*, and *grn* (Figures 4H and S4B). We normalized proximity maps by the proximity frequencies in the head, where the anchor exhibited maximal expression (Figure 4H). Notably, normalized proximity frequencies were negative for the majority of segments and targets (Figures 4H, 4I–4L, and S6E). Thus, and in contrast to *Hox* Pc targets, non-*Hox* Pc targets displayed the highest proximity frequencies in regions where they are co-expressed. All in all, our results show that proximity frequencies of distant Pc targets are spatially modulated and can be tuned in different cell types by co-repression as well as by co-expression.

DISCUSSION

Previous evidence suggested that multiple Pc TADs may often associate with each other in single cells to form Pc compartments (bodies) to reinforce gene repression.^{48–50} Here, we investigated the nature of these compartments by implementing a multiplexed imaging-based approach that maps the multiscale

(H) Violin plots display the normalized proximity frequency distributions of non-*Hox* target genes with all other Pc barcodes in chr3R. Proximity frequencies were normalized by the segment of expression of each non-*Hox* gene. Error bars represent standard deviations.

(I–L) Normalized proximity frequency maps for different non-*Hox* targets and anchors: *grn* (I), *ems* (J), *hth* (K), and *svp* (L). Proximity frequencies were normalized with respect to a segment displaying anchor expression.

organization of Pc target genes in different presumptive tissues within the *Drosophila* embryo.

Pairs of Pc target genes are able to interact in 3D by “gene kissing,” an activity that requires Pc components and possibly other factors, such as chromatin insulators.^{4,19} The ability of our approach to detect multiple Pc target genes in single cells allowed us to shed light into the nature of these kissing interactions. Previous studies determined that interactions between pairs of distant *Hox* genes were rare (10%–20%) and proposed that the existence of multiple accessible Pc partners may explain why two *Hox* genes only interact in a small fraction of nuclei.^{4,19} In fact, our analysis shows that spatial colocalization of any two distant intra-chromosomal Pc targets is rather infrequent. These results are consistent with a recent single-nucleus Hi-C study in *Drosophila* BG3 cells showing a weak enrichment in long-range interactions between Pc repressed regions.⁵¹ Moreover, we show that these rare long-range interactions require Pc components and are acquired after the emergence of TADs at NC14^{25,28} and concomitant with the enrichment of Pc compartments.⁵² These observations are consistent with homotypic interactions between Pc domains being mainly mediated by the biochemical properties of the Pc complexes, including the oligomerization property of the SAM domain of PH and the spreading faculty of Pc on the H3K27me3 chromatin mark. Notably, our data show that frequencies of long-range interactions vary widely between targets and do not only depend on genomic distance, suggesting a role for additional factors (e.g., insulators) in the modulation of interaction specificity.

Previous genome-wide studies showed extensive interactions between distant Pc genes,¹⁹ raising the possibility that Pc repressive compartments could involve the coalescence of multiple repressed genomic regions. We tested this hypothesis by directly calculating the frequency of pairwise versus multi-way interactions. Notably, we found that binary interactions are predominant, with the frequency of multi-way contacts drastically decreasing with the number of targets. This finding is consistent with previous imaging studies showing that Pc TADs often appear as discrete 3D chromosomal units.¹⁵ This predominance of pairwise interactions may arise due to physical constraints on the overall folding of the chromosome within the nucleus (e.g., co-localization of centromeres/telomeres) or from associations of other compartment types (e.g., black, active) limiting the association of multiple Pc targets into compartments. We note that, even in the case of large domains containing multiple Pc target genes (i.e., ANT-C and BX-C), 2-way contacts are dominant over 3-way contacts (Figure 3F), suggesting that Pc target genes within Pc domains do not colocalize often in 3D. Our study only investigates 3D interactions between Pc domains located in chr3R, where the density of Pc targets is high. Nonetheless, we do not expect to observe higher frequencies of multi-way interactions, given that *Drosophila* chromosomes occupy discrete nuclear compartments⁴² and that Pc targets interact more frequently with targets in their own chromosomal arm.⁴

These results are supported by polymer modeling, where the globule regime correctly captures the behavior of Pc domains. This polymer is close to the θ -like transition in the phase diagram. In this configuration, a small change in the interaction energy between monomers leads to a large change in the overall energy of

the polymer, allowing chromatin to switch conformation easily with a small difference in interaction energies. This behavior is consistent with the dynamic occupancy of Pc sites by PRC1 proteins, observed both in *Drosophila* and mammals,^{53–56} and with a recent single-nucleus Hi-C study showing that long-range Pc contacts occur regardless of their genomic distance.⁵¹ Furthermore, this behavior is maintained in Pc mutants, consistent with other factors (HP1, insulators, transcription hubs, or other PcG protein subunits) also likely contributing to the long-range organization of Pc domains^{25,42,43,51,57} and providing a scaffold that facilitates the encounter of distant Pc domains. In addition, our polymer model correctly captures the behavior of Pc domains, notably the predominantly pairwise nature of interacting partners, and the correlation between Pc architecture and gene expression. Overall, our experiments and simulations suggest that Pc repressive compartments form by infrequent associations of Pc domains. PRC1 proteins play an important role in the formation of these compartments; however, other factors, such as the entropy of the chromatin polymer, specific contacts mediated by other chromatin factors, and attractive interactions between active or repressed regions, are also relevant.

To investigate what processes may modulate long-range Pc interactions, we resorted to the ability of our method to reconstruct chromatin architecture in embryonic segments with different epigenetic and transcriptional states. Remarkably, we found that proximity frequencies between Pc targets are modulated by both transcriptional repression and activation. *Hox* genes were colocalized most frequently in segments where they were co-repressed, both for targets located within the same TAD or for very distant genes. This result was consistent with previous observations on a limited number of targets.^{19,20,36} Notably, transcriptional activation of *Hox* genes led to their spatial segregation, locally from other Pc targets within their TAD and more globally from other repressed distant Pc targets. Finally, non-*Hox* genes more frequently colocalized in regions where they were both expressed, consistent with previous observations on a limited number of targets.⁵⁸ These interactions among co-expressed genes might depend on trithorax-group factors that can physically interact with Pc components to activate gene expression.^{59–61}

In conclusion, our data are inconsistent with repressive Pc compartments being formed by the extensive coalescence of multiple distant Pc regions and instead show that interactions between Pc genes occur infrequently and involve mostly pairwise encounters modulated by transcriptional status.

Limitations of the study

We identified the following limitations in our study. First, we measure the proximity frequencies between a selection of Pc targets in chr3R. While we expect similar results for Pc targets in other chromosome arms, further studies will be required to show it. Similarly, genome-wide data support our hypothesis that Pc targets interact more often with Pc targets within the same chromosomal arm than within Pc targets in other arms. Thus, additional single-cell studies will be required to dissect the frequencies and mode of inter-chromosomal Pc interactions. Second, the barcode detection efficiency for confocal-based Hi-M in late-stage embryos is ~45%; therefore, the number of complete chromatin

traces is low. This prevents more complex single-cell analysis of 3D chromatin conformation, where most (or all) barcode positions are needed. Third, we observe that, on average, Pc targets tend to co-localize more frequently in regions where they are both repressed. However, our study does not image histone marks and chromatin organization simultaneously, a measurement that would be important to establish a causal link between epigenetic state and chromatin organization as well as to identify the sources of variation in 3D chromatin organization. Finally, we observe that non-*Hox* genes tend to co-localize more frequently in regions where both genes are expressed. However, our experiments do not detect transcription spots and 3D organization simultaneously, therefore preventing us from making a causal link between co-expression and co-localization or from dissecting the heterogeneity in this process.

STAR★METHODS

Detailed methods are provided in the online version of this paper and include the following:

- [KEY RESOURCES TABLE](#)
- [RESOURCES AVAILABILITY](#)
 - Lead contact
 - Material availability
 - Data and code availability
- [EXPERIMENTAL MODEL AND STUDY PARTICIPANT DETAILS](#)
- [METHOD DETAILS](#)
 - Probe selection and library design
 - Library synthesis and amplification
 - Adaptor and imaging oligos
 - Embryo collection and fixation
 - Hybridization of Hi-M library
 - Microscope setup
 - Image acquisition
 - Polymer modeling
- [QUANTIFICATION AND STATISTICAL ANALYSIS](#)
 - Data analysis

SUPPLEMENTAL INFORMATION

Supplemental information can be found online at <https://doi.org/10.1016/j.celrep.2024.114167>.

ACKNOWLEDGMENTS

This project was funded by the European Union's Horizon 2020 Research and Innovation Program (grant ID 724429) (to M.N.). We acknowledge the Bettencourt Schueller Foundation for their prize "Coup d'élan pour la recherche Française," the France-Biomedicine infrastructure supported by the French National Research Agency (grant ID ANR-10-INBS-04, "Investments for the Future"), and the *Drosophila* facility (BioCampus Montpellier, CNRS, INSERM, Université Montpellier, Montpellier, France).

AUTHOR CONTRIBUTIONS

Conceptualization, J.G., F.B., and M.N.; methodology, J.G., C.H., J.-B.F., J.-C.W., and M.N.; investigation, J.G., J.-C.W., F.B., and M.N.; writing – original draft, J.G. and M.N.; writing – review & editing, J.G., J.-C.W., J.-B.F., M.S., G.C., F.B., and M.N.; funding acquisition, M.N.; resources, J.G., C.H., J.-B.F., M.S., and F.B.; supervision, F.B. and M.N.

DECLARATION OF INTERESTS

The authors declare no competing interests.

Received: April 22, 2022
Revised: February 15, 2024
Accepted: April 12, 2024
Published: April 30, 2024

REFERENCES

1. Lieberman-Aiden, E., van Berkum, N.L., Williams, L., Imakaev, M., Ragozcy, T., Telling, A., Amit, I., Lajoie, B.R., Sabo, P.J., Dorschner, M.O., et al. (2009). Comprehensive Mapping of Long-Range Interactions Reveals Folding Principles of the Human Genome. *Science* 326, 289–293. <https://doi.org/10.1126/science.1181369>.
2. Dixon, J.R., Selvaraj, S., Yue, F., Kim, A., Li, Y., Shen, Y., Hu, M., Liu, J.S., and Ren, B. (2012). Topological domains in mammalian genomes identified by analysis of chromatin interactions. *Nature* 485, 376–380. <https://doi.org/10.1038/nature11082>.
3. Nora, E.P., Lajoie, B.R., Schulz, E.G., Giorgetti, L., Okamoto, I., Servant, N., Piolot, T., van Berkum, N.L., Meisig, J., Sedat, J., et al. (2012). Spatial partitioning of the regulatory landscape of the X-inactivation centre. *Nature* 485, 381–385. <https://doi.org/10.1038/nature11049>.
4. Sexton, T., Yaffe, E., Kenigsberg, E., Bantignies, F., Leblanc, B., Hoichman, M., Parrinello, H., Tanay, A., and Cavalli, G. (2012). Three-Dimensional Folding and Functional Organization Principles of the Drosophila Genome. *Cell* 148, 458–472. <https://doi.org/10.1016/j.cell.2012.01.010>.
5. Hou, C., Li, L., Qin, Z.S., and Corces, V.G. (2012). Gene Density, Transcription, and Insulators Contribute to the Partition of the Drosophila Genome into Physical Domains. *Mol. Cell* 48, 471–484. <https://doi.org/10.1016/j.molcel.2012.08.031>.
6. Cavalli, G., and Misteli, T. (2013). Functional implications of genome topology. *Nat. Struct. Mol. Biol.* 20, 290–299. <https://doi.org/10.1038/nsmb.2474>.
7. Andrey, G., and Mundlos, S. (2017). The three-dimensional genome: regulating gene expression during pluripotency and development. *Development* 144, 3646–3658. <https://doi.org/10.1242/dev.148304>.
8. Szabo, Q., Bantignies, F., and Cavalli, G. (2019). Principles of genome folding into topologically associating domains. *Sci. Adv.* 5, eaaw1668. <https://doi.org/10.1126/sciadv.aaw1668>.
9. Nègre, N., Hennetin, J., Sun, L.V., Lavrov, S., Bellis, M., White, K.P., and Cavalli, G. (2006). Chromosomal Distribution of PcG Proteins during Drosophila Development. *PLoS Biol.* 4, e170. <https://doi.org/10.1371/journal.pbio.0040170>.
10. Wang, L., Brown, J.L., Cao, R., Zhang, Y., Kassiss, J.A., and Jones, R.S. (2004). Hierarchical Recruitment of Polycomb Group Silencing Complexes. *Mol. Cell* 14, 637–646. <https://doi.org/10.1016/j.molcel.2004.05.009>.
11. Francis, N.J., Kingston, R.E., and Woodcock, C.L. (2004). Chromatin Compaction by a Polycomb Group Protein Complex. *Science* 306, 1574–1577. <https://doi.org/10.1126/science.1100576>.
12. Grau, D.J., Chapman, B.A., Garlick, J.D., Borowsky, M., Francis, N.J., and Kingston, R.E. (2011). Compaction of chromatin by diverse Polycomb group proteins requires localized regions of high charge. *Genes Dev.* 25, 2210–2221. <https://doi.org/10.1101/gad.17288211>.
13. Boettiger, A.N., Bintu, B., Moffitt, J.R., Wang, S., Beliveau, B.J., Fudenberg, G., Imakaev, M., Mirny, L.A., Wu, C.t., and Zhuang, X. (2016). Super-resolution imaging reveals distinct chromatin folding for different epigenetic states. *Nature* 529, 418–422. <https://doi.org/10.1038/nature16496>.
14. Wani, A.H., Boettiger, A.N., Schorderet, P., Ergun, A., Münger, C., Sadréyev, R.I., Zhuang, X., Kingston, R.E., and Francis, N.J. (2016).

- Chromatin topology is coupled to Polycomb group protein subnuclear organization. *Nat. Commun.* 7, 10291. <https://doi.org/10.1038/ncomms10291>.
15. Szabo, Q., Jost, D., Chang, J.-M., Cattoni, D.I., Papadopoulos, G.L., Bonev, B., Sexton, T., Gurgo, J., Jacquier, C., Nollmann, M., et al. (2018). TADs are 3D structural units of higher-order chromosome organization in *Drosophila*. *Sci. Adv.* 4, eaar8082. <https://doi.org/10.1126/sciadv.aar8082>.
 16. Mateo, L.J., Murphy, S.E., Hafner, A., Cinquini, I.S., Walker, C.A., and Boettiger, A.N. (2019). Visualizing DNA folding and RNA in embryos at single-cell resolution. *Nature* 568, 49–54. <https://doi.org/10.1038/s41586-019-1035-4>.
 17. Saurin, A.J., Shiels, C., Williamson, J., Satijn, D.P., Otte, A.P., Sheer, D., and Freemont, P.S. (1998). The Human Polycomb Group Complex Associates with Pericentromeric Heterochromatin to Form a Novel Nuclear Domain. *J. Cell Biol.* 142, 887–898. <https://doi.org/10.1083/jcb.142.4.887>.
 18. Buchenau, P., Hodgson, J., Strutt, H., and Arndt-Jovin, D.J. (1998). The Distribution of Polycomb-Group Proteins During Cell Division and Development in *Drosophila* Embryos: Impact on Models for Silencing. *J. Cell Biol.* 141, 469–481. <https://doi.org/10.1083/jcb.141.2.469>.
 19. Bantignies, F., Roure, V., Comet, I., Leblanc, B., Schuettengruber, B., Bonnet, J., Tixier, V., Mas, A., and Cavalli, G. (2011). Polycomb-Dependent Regulatory Contacts between Distant Hox Loci in *Drosophila*. *Cell* 144, 214–226. <https://doi.org/10.1016/j.cell.2010.12.026>.
 20. Lanzuolo, C., Roure, V., Dekker, J., Bantignies, F., and Orlando, V. (2007). Polycomb response elements mediate the formation of chromosome higher-order structures in the bithorax complex. *Nat. Cell Biol.* 9, 1167–1174. <https://doi.org/10.1038/ncb1637>.
 21. Cattoni, D.I., Cardozo Gizzi, A.M., Georgieva, M., Di Stefano, M., Valeri, A., Chamousset, D., Houbron, C., Déjardin, S., Fiche, J.-B., González, I., et al. (2017). Single-cell absolute contact probability detection reveals chromosomes are organized by multiple low-frequency yet specific interactions. *Nat. Commun.* 8, 1753. <https://doi.org/10.1038/s41467-017-01962-x>.
 22. Cardozo Gizzi, A.M., Cattoni, D.I., Fiche, J.-B., Espinola, S.M., Gurgo, J., Messina, O., Houbron, C., Ogiyama, Y., Papadopoulos, G.L., Cavalli, G., et al. (2019). Microscopy-Based Chromosome Conformation Capture Enables Simultaneous Visualization of Genome Organization and Transcription in Intact Organisms. *Mol. Cell* 74, 212–222.e5. <https://doi.org/10.1016/j.molcel.2019.01.011>.
 23. Cardozo Gizzi, A.M., Espinola, S.M., Gurgo, J., Houbron, C., Fiche, J.-B., Cattoni, D.I., and Nollmann, M. (2020). Direct and simultaneous observation of transcription and chromosome architecture in single cells with Hi-M. *Nat. Protoc.* 15, 840–876. <https://doi.org/10.1038/s41596-019-0269-9>.
 24. Tolhuis, B., Blom, M., Kerkhoven, R.M., Pagie, L., Teunissen, H., Nieuwland, M., Simonis, M., de Laat, W., van Lohuizen, M., and van Steensel, B. (2011). Interactions among Polycomb Domains Are Guided by Chromosome Architecture. *PLoS Genet.* 7, e1001343. <https://doi.org/10.1371/journal.pgen.1001343>.
 25. Hug, C.B., Grimaldi, A.G., Kruse, K., and Vaquerizas, J.M. (2017). Chromatin Architecture Emerges during Zygotic Genome Activation Independent of Transcription. *Cell* 169, 216–228.e19. <https://doi.org/10.1016/j.cell.2017.03.024>.
 26. Ing-Simmons, E., Vaid, R., Bing, X.Y., Levine, M., Mannervik, M., and Vaquerizas, J.M. (2021). Independence of chromatin conformation and gene regulation during *Drosophila* dorsoventral patterning. *Nat. Genet.* 53, 487–499. <https://doi.org/10.1038/s41588-021-00799-x>.
 27. Loubiere, V., Papadopoulos, G.L., Szabo, Q., Martinez, A.-M., and Cavalli, G. (2020). Widespread activation of developmental gene expression characterized by PRC1-dependent chromatin looping. *Sci. Adv.* 6, eaax4001. <https://doi.org/10.1126/sciadv.aax4001>.
 28. Ogiyama, Y., Schuettengruber, B., Papadopoulos, G.L., Chang, J.-M., and Cavalli, G. (2018). Polycomb-Dependent Chromatin Looping Contributes to Gene Silencing during *Drosophila* Development. *Mol. Cell* 71, 73–88.e5. <https://doi.org/10.1016/j.molcel.2018.05.032>.
 29. Beliveau, B.J., Boettiger, A.N., Avendaño, M.S., Jungmann, R., McCole, R.B., Joyce, E.F., Kim-Kiselak, C., Bantignies, F., Fonseka, C.Y., Erceg, J., et al. (2015). Single-molecule super-resolution imaging of chromosomes and in situ haplotype visualization using Oligopaint FISH probes. *Nat. Commun.* 6, 7147. <https://doi.org/10.1038/ncomms8147>.
 30. Beliveau, B.J., Joyce, E.F., Apostolopoulos, N., Yilmaz, F., Fonseka, C.Y., McCole, R.B., Chang, Y., Li, J.B., Senaratne, T.N., Williams, B.R., et al. (2012). Versatile design and synthesis platform for visualizing genomes with Oligopaint FISH probes. *Proc. Natl. Acad. Sci. USA* 109, 21301–21306.
 31. Bintu, B., Mateo, L.J., Su, J.-H., Sinnott-Armstrong, N.A., Parker, M., Kinrot, S., Yamaya, K., Boettiger, A.N., and Zhuang, X. (2018). Super-resolution chromatin tracing reveals domains and cooperative interactions in single cells. *Science* 362, eaau1783. <https://doi.org/10.1126/science.aau1783>.
 32. Takeji, Y., Yun, J., Zheng, S., Ollikainen, N., Pierson, N., White, J., Shah, S., Thomassie, J., Suo, S., Eng, C.-H.L., et al. (2021). Integrated spatial genomics reveals global architecture of single nuclei. *Nature* 590, 344–350. <https://doi.org/10.1038/s41586-020-03126-2>.
 33. Su, J.-H., Zheng, P., Kinrot, S.S., Bintu, B., and Zhuang, X. (2020). Genome-Scale Imaging of the 3D Organization and Transcriptional Activity of Chromatin. *Cell* 182, 1641–1659.e26. <https://doi.org/10.1016/j.cell.2020.07.032>.
 34. Nir, G., Farabella, I., Pérez Estrada, C., Ebeling, C.G., Beliveau, B.J., Sasaki, H.M., Lee, S.D., Nguyen, S.C., McCole, R.B., Chatteraj, S., et al. (2018). Walking along chromosomes with super-resolution imaging, contact maps, and integrative modeling. *PLoS Genet.* 14, e1007872.
 35. Liu, M., Lu, Y., Yang, B., Chen, Y., Radda, J.S.D., Hu, M., Katz, S.G., and Wang, S. (2020). Multiplexed imaging of nucleome architectures in single cells of mammalian tissue. *Nat. Commun.* 11, 2907. <https://doi.org/10.1038/s41467-020-16732-5>.
 36. Cheutin, T., and Cavalli, G. (2018). Loss of PRC1 induces higher-order opening of Hox loci independently of transcription during *Drosophila* embryogenesis. *Nat. Commun.* 9, 3898. <https://doi.org/10.1038/s41467-018-05945-4>.
 37. Mirny, L.A. (2011). The fractal globule as a model of chromatin architecture in the cell. *Chromosome Res.* 19, 37–51. <https://doi.org/10.1007/s10577-010-9177-0>.
 38. Halverson, J.D., Smrek, J., Kremer, K., and Grosberg, A.Y. (2014). From a melt of rings to chromosome territories: the role of topological constraints in genome folding. *Rep. Prog. Phys.* 77, 022601. <https://doi.org/10.1088/0034-4885/77/2/022601>.
 39. Jost, D., Carrivain, P., Cavalli, G., and Vaillant, C. (2014). Modeling epigenome folding: formation and dynamics of topologically associated chromatin domains. *Nucleic Acids Res.* 42, 9553–9561. <https://doi.org/10.1093/nar/gku698>.
 40. Leibler, L. (1980). Theory of Microphase Separation in Block Copolymers. *Macromolecules* 13, 1602–1617. <https://doi.org/10.1021/ma60078a047>.
 41. Haddad, N., Jost, D., and Vaillant, C. (2017). Perspectives: using polymer modeling to understand the formation and function of nuclear compartments. *Chromosome Res.* 25, 35–50. <https://doi.org/10.1007/s10577-016-9548-2>.
 42. Zenk, F., Zhan, Y., Kos, P., Löser, E., Atinbayeva, N., Schächtle, M., Tiana, G., Giorgetti, L., and Iovino, N. (2021). HP1 drives de novo 3D genome reorganization in early *Drosophila* embryos. *Nature* 593, 289–293. <https://doi.org/10.1038/s41586-021-03460-z>.
 43. Rowley, M.J., Nichols, M.H., Lyu, X., Ando-Kuri, M., Rivera, I.S.M., Hermetz, K., Wang, P., Ruan, Y., and Corces, V.G. (2017). Evolutionarily Conserved Principles Predict 3D Chromatin Organization. *Mol. Cell* 67, 837–852.e7. <https://doi.org/10.1016/j.molcel.2017.07.022>.
 44. Lewis, E.B. (1978). A gene complex controlling segmentation in *Drosophila*. *Nature* 276, 565–570. <https://doi.org/10.1038/276565a0>.

45. Dessain, S., and McGinnis, W. (1993). Drosophila Homeobox Genes. In *Advances in Developmental Biochemistry* Advances in Developmental Biochemistry, P.M. Wassarman, ed. (Academic Press), pp. 1–55. [https://doi.org/10.1016/S1064-2722\(08\)60035-3](https://doi.org/10.1016/S1064-2722(08)60035-3).
46. Lewis, E.B., Pfeiffer, B.D., Mathog, D.R., and Celniker, S.E. (2004). Evolution of the Homeobox Complex in the Diptera. In *Genes, Development and Cancer: The Life and Work of Edward B. Lewis, H.D. Lipshitz*, ed. (Springer US), pp. 381–385. https://doi.org/10.1007/978-1-4419-8981-9_24.
47. Kaufman, T.C., Seeger, M.A., and Olsen, G. (1990). Molecular and Genetic Organization of The Antennapedia Gene Complex of *Drosophila melanogaster*. In *Advances in Genetics Genetic Regulatory Hierarchies in Development*, T.R.F. Wright, ed. (Academic Press), pp. 309–362. [https://doi.org/10.1016/S0065-2660\(08\)60029-2](https://doi.org/10.1016/S0065-2660(08)60029-2).
48. Isono, K., Endo, T.A., Ku, M., Yamada, D., Suzuki, R., Sharif, J., Ishikura, T., Toyoda, T., Bernstein, B.E., and Koseki, H. (2013). SAM Domain Polymerization Links Subnuclear Clustering of PRC1 to Gene Silencing. *Dev. Cell* 26, 565–577. <https://doi.org/10.1016/j.devcel.2013.08.016>.
49. Delest, A., Sexton, T., and Cavalli, G. (2012). Polycomb: a paradigm for genome organization from one to three dimensions. *Curr. Opin. Cell Biol.* 24, 405–414. <https://doi.org/10.1016/j.ceb.2012.01.008>.
50. Bantignies, F., and Cavalli, G. (2011). Polycomb group proteins: repression in 3D. *Trends Genet.* 27, 454–464. <https://doi.org/10.1016/j.tig.2011.06.008>.
51. Ulianov, S.V., Zakharova, V.V., Galitsyna, A.A., Kos, P.I., Polovnikov, K.E., Flyamer, I.M., Mikhaleva, E.A., Khrameeva, E.E., Germini, D., Logacheva, M.D., et al. (2021). Order and stochasticity in the folding of individual *Drosophila* genomes. *Nat. Commun.* 12, 41. <https://doi.org/10.1038/s41467-020-20292-z>.
52. Cheutin, T., and Cavalli, G. (2012). Progressive Polycomb Assembly on H3K27me3 Compartments Generates Polycomb Bodies with Developmentally Regulated Motion. *PLoS Genet.* 8, e1002465. <https://doi.org/10.1371/journal.pgen.1002465>.
53. Ficiz, G., Heintzmann, R., and Arndt-Jovin, D.J. (2005). Polycomb group protein complexes exchange rapidly in living *Drosophila*. *Development* 132, 3963–3976. <https://doi.org/10.1242/dev.01950>.
54. Fonseca, J.P., Steffen, P.A., Müller, S., Lu, J., Sawicka, A., Seiser, C., and Ringrose, L. (2012). In vivo Polycomb kinetics and mitotic chromatin binding distinguish stem cells from differentiated cells. *Genes Dev.* 26, 857–871. <https://doi.org/10.1101/gad.184648.111>.
55. Steffen, P.A., Fonseca, J.P., Gänger, C., Dworschak, E., Kockmann, T., Beisel, C., and Ringrose, L. (2013). Quantitative in vivo analysis of chromatin binding of Polycomb and Trithorax group proteins reveals retention of ASH1 on mitotic chromatin. *Nucleic Acids Res.* 41, 5235–5250. <https://doi.org/10.1093/nar/gkt217>.
56. Huseyin, M.K., and Klose, R.J. (2021). Live-cell single particle tracking of PRC1 reveals a highly dynamic system with low target site occupancy. *Nat. Commun.* 12, 887. <https://doi.org/10.1038/s41467-021-21130-6>.
57. Tuszyńska, I., Bednarz, P., and Wilczynski, B. (2024). Black chromatin is indispensable for accurate simulations of *Drosophila melanogaster* chromatin structure. *J Biomol Struct Dyn.* <https://doi.org/10.1080/07391102.2023.2291176>.
58. Li, H.-B., Ohno, K., Gui, H., and Pirrotta, V. (2013). Insulators Target Active Genes to Transcription Factories and Polycomb-Repressed Genes to Polycomb Bodies. *PLoS Genet.* 9, e1003436. <https://doi.org/10.1371/journal.pgen.1003436>.
59. Strübbe, G., Popp, C., Schmidt, A., Pauli, A., Ringrose, L., Beisel, C., and Paro, R. (2011). Polycomb purification by in vivo biotinylation tagging reveals cohesin and Trithorax group proteins as interaction partners. *Proc. Natl. Acad. Sci. USA* 108, 5572–5577. <https://doi.org/10.1073/pnas.1007916108>.
60. Kadoch, C., Williams, R.T., Calarco, J.P., Miller, E.L., Weber, C.M., Braun, S.M.G., Pulice, J.L., Chory, E.J., and Crabtree, G.R. (2017). Dynamics of BAF–Polycomb complex opposition on heterochromatin in normal and oncogenic states. *Nat. Genet.* 49, 213–222. <https://doi.org/10.1038/ng.3734>.
61. Stanton, B.Z., Hodges, C., Calarco, J.P., Braun, S.M.G., Ku, W.L., Kadoch, C., Zhao, K., and Crabtree, G.R. (2017). Smarca4 ATPase mutations disrupt direct eviction of PRC1 from chromatin. *Nat. Genet.* 49, 282–288. <https://doi.org/10.1038/ng.3735>.
62. Schuettengruber, B., Oded Elkayam, N., Sexton, T., Entrevan, M., Stern, S., Thomas, A., Yaffe, E., Parrinello, H., Tanay, A., and Cavalli, G. (2014). Cooperativity, specificity, and evolutionary stability of Polycomb targeting in *Drosophila*. *Cell Rep.* 9, 219–233. <https://doi.org/10.1016/j.celrep.2014.08.072>.
63. Franke, A., Messmer, S., and Paro, R. (1995). Mapping functional domains of the Polycomb protein of *Drosophila melanogaster*. *Chromosome Res.* 3, 351–360. <https://doi.org/10.1007/BF00710016>.
64. Barho, F., Fiche, J.-B., Bardou, M., Messina, O., Martiniere, A., Houbbron, C., and Nollmann, M. (2022). Qudi-HiM: an open-source acquisition software package for highly multiplexed sequential and combinatorial optical imaging. *Open Res. Eur.* 2, 46. <https://doi.org/10.12688/openreseurope.14641.2>.
65. Walter, J.-C., and Barkema, G.T. (2015). An introduction to Monte Carlo methods. *Phys. Stat. Mech. Its Appl.* 418, 78–87. <https://doi.org/10.1016/j.physa.2014.06.014>.
66. Sakaue, T., Walter, J.-C., Carlon, E., and Vanderzande, C. (2017). Non-Markovian dynamics of reaction coordinate in polymer folding. *Soft Matter* 13, 3174–3181. <https://doi.org/10.1039/C7SM00395A>.
67. Walter, J.-C., Baiesi, M., Barkema, G.T., and Carlon, E. (2013). Unwinding Relaxation Dynamics of Polymers. *Phys. Rev. Lett.* 110, 068301. <https://doi.org/10.1103/PhysRevLett.110.068301>.
68. Schneider, C.A., Rasband, W.S., and Eliceiri, K.W. (2012). NIH Image to ImageJ: 25 years of image analysis. *Nat. Methods* 9, 671–675. <https://doi.org/10.1038/nmeth.2089>.
69. Schindelin, J., Arganda-Carreras, I., Frise, E., Kaynig, V., Longair, M., Pietzsch, T., Preibisch, S., Rueden, C., Saalfeld, S., Schmid, B., et al. (2012). Fiji: an open-source platform for biological-image analysis. *Nat. Methods* 9, 676–682. <https://doi.org/10.1038/nmeth.2019>.
70. Linkert, M., Rueden, C.T., Allan, C., Burel, J.-M., Moore, W., Patterson, A., Loranger, B., Moore, J., Neves, C., MacDonald, D., et al. (2010). Metadata matters: access to image data in the real world. *J. Cell Biol.* 189, 777–782. <https://doi.org/10.1083/jcb.201004104>.
71. Devos, X., Fiche, J.-B., Bardou, M., Messina, O., Houbbron, C., Gurgo, J., Schaeffer, M., Götz, M., Walter, T., Mueller, F., and Nollmann, M. (2024). pyHiM: a new open-source, multi-platform software package for spatial genomics based on multiplexed DNA-FISH imaging. *Genome Biol.* 25, 47. <https://doi.org/10.1186/s13059-024-03178-x>.

STAR★METHODS

KEY RESOURCES TABLE

REAGENT or RESOURCE	SOURCE	IDENTIFIER
Critical commercial assays		
DNA Clean & Concentrator-100	Zymo Research	D4029
DNA Clean & Concentrator-25	Zymo Research	D4033
Oligo Clean & Concentrator	Zymo Research	D4060
HiScribe T7 High Yield RNA Synthesis Kit	New England Biolabs	E2040S
Transcriptase inverse Maxima H Minus	Thermo Scientific	EP0753
Deposited data		
Hi-M datasets	OSF	https://doi.org/10.17605/OSF.IO/Y8CRA
Experimental models: Organisms/strains		
Drosophila Melanogaster wild-type	Bloomington Drosophila Stock Center (BDSC)	Oregon-R w[1118] FlyBase: FBa0018186
Drosophila Melanogaster Pc mutant	Bloomington Drosophila Stock Center (BDSC)	Pc[XT109] or Pc[15], BS: 24468
Drosophila Melanogaster balancer	Bloomington Drosophila Stock Center (BDSC)	KrGFP-TM3, Sb[1] balancer, BS: 5195
Oligonucleotides		
barcode imager 5'-CACACGCTCTTCCGTTCTA TGCGACGTCGGTG/iThioMC6-D//3A1exF647N/	Integrated DNA Technologies	N/A
fiducial imager 5'-CATTGCCGTATGGGCTAGG ATGACCTGGCTCG/3RhodRd-XN/	Integrated DNA Technologies	N/A
displacement oligo 5'-CAACTCATGCTTAGTCTCG TCGCAACGCCAGG	Integrated DNA Technologies	N/A
reverse primer 5'-GTGTCCGAGGCTGTCTCCTAG	Integrated DNA Technologies	N/A
forward primer 5'-CAGGTCGAGCCCTGTAGTACG	Integrated DNA Technologies	N/A
Software and algorithms		
MATLAB	The MathWorks, Inc., Natick, United States	2019b
Huygens	Scientific Volume Imaging, the Netherlands	Professional version 20.04
HiM acquisition Labview	Github	https://github.com/HiM-public-resources/HiMacquisitionSoft
Qudi-HiM	Zenodo	https://doi.org/10.5281/zenodo.6379944
HiM analysis MATLAB	Mendeley	https://doi.org/10.17632/5f5hd9yj3z.1
pyHiM	OSF	https://doi.org/10.17605/OSF.IO/UPDFW

RESOURCES AVAILABILITY

Lead contact

Further information and requests for resources and reagents should be directed to and will be fulfilled by the lead contact, Marcelo Nollmann (marcelo.nollmann@cbs.cnrs.fr).

Material availability

This study did not generate unique reagents.

Data and code availability

- Hi-M data have been deposited at [Open Science Framework](#) and are publicly available as of the date of publication. DOIs are listed in the [key resources table](#).

- This paper does not report original code.
- Any additional information required to reanalyze the data reported in this paper is available from the [lead contact](#) upon request.

EXPERIMENTAL MODEL AND STUDY PARTICIPANT DETAILS

Our studies were performed on *Drosophila melanogaster* embryos (strain: wild-type Oregon-R), staged at nuclear cycle 14, or at Stage 15–16. Both male and female embryos were used, therefore our study cannot discern differences between the two.

METHOD DETAILS

Probe selection and library design

A portion of ~15 Mb of chromosome 3R was selected. A 3 node self-organizing map (SOM, ‘kohonen’ R package) was used to produce a 3-way segmentation of 10 kb genome wide bins. Each bin was scored based on the average ChIP-seq read counts of H3K27me3, H3K4me3 and H3K36me3 from 14 to 16 h embryos (modEncode, 3955 H3K27me3, Embryos-14-16 h, OregonR, ChIP-seq; modEncode, 5096: H3K4me3, Oregon-R, Embryos 14–16 h OR, ChIP-seq; 4950: H3K36me3, Oregon-R, Embryos 14–16 h OR, ChIP-seq). Each SOM node was treated as a discrete cluster and contiguous bins assigned to the same node were merged into one epi-domain. Only epi-domains of a size equal or bigger to 20 kb were selected. To find Pc domains, we further filtered epi-domains by their enrichment in H3K27me3 (modEncode, 3955 H3K27me3, Embryos-14-16 h; OregonR; ChIP-seq), in PRC1 subunits (PC, PH) for embryos of 16–18 h of development (accession number GSE60428),⁶² and for PSC (modEncode, 3960: Psc; Oregon-R; Embryos 14–16 h OR; ChIP-seq, *D. melanogaster*). Only domains with peaks for the three PRC1 subunits (PH, PC, PSC) were kept. Long-range interactions between these domains were also visually inspected using Hi-C maps from.²⁸ For active domains, they were re-selected based on the enrichment of H3K4me3 and H3K36me3 (modEncode, 5096: H3K4me3; Oregon-R; Embryos 14–16 h OR; ChIP-seq; 4950: H3K36me3; Oregon-R; Embryos 14–16 h OR; ChIP-seq), and were also visually inspected using Hi-C maps from.²⁸ For inactive domains, they were selected based on the absence of the aforementioned epigenetic marks. Domains between 20 and 100 kb were labeled by one 15 kb probe, centered in the middle of the domain, for all domain types. Domains between 100 and 200 kb were labeled by two 15 kb probes centered at PcG protein peaks for Pc domains, and two 15 kb domains homogeneously distributed for active and inactive domains. Domains bigger than 200 kb comprise ANTP-C, BX-C and NK-C, and are labeled by 15 kb probes targeting the promoters of their genes (5,3 and 3 probes respectively). The selected Polycomb targets correspond to the PcG targets in Chromosome 3R displaying the large majority of interactions (Bantignies, 2011). Polycomb domains located outside the selected ~15 Mb region, or smaller than 20 kb were not labeled as they interacted with other Polycomb genes very infrequently.

Library synthesis and amplification

The library synthesis method is based on the developments of Beliveau and colleagues.^{29,30} After selecting the genomic regions of interest, a database of genomically unique, non-overlapping sequences was used to generate the Oligopaint primary probes library (Oligopaints website: <https://oligopaints.hms.harvard.edu/>). Each oligo of the primary library is made of 148 nucleotides (nt), and consists in (from 5' to 3'): a 22 nt forward universal primer region for library amplification, two concatenated 20 nt readout regions, unique to each 15 kb targeted region, and separated by a 2-nt spacer, a 42 nt region of homology to genomic DNA, a second 20 nt readout region (identical to the first), and a 22 nt unique reverse primer for library amplification. An Oligopool with all the nucleotides used was ordered from Custom Array.

The procedure to amplify the library consists in four main steps: (1) PCR amplification of the Oligopaints library using a reverse primer that adds the T7 promoter sequence; (2) Conversion of the PCR product to RNA via an *in vitro* transcription using T7 polymerase; (3) Generation of single-stranded DNA (ssDNA) via reverse transcription; (4) Degradation of the RNA template using alkaline hydrolysis. The full protocol can be found at.²³

Coordinates for the barcodes imaged in this study are provided in [Table S1](#). Sequences for the oligopaint primary library are provided in [Table S2](#). Primer sequences for library amplification are listed in the Key Resources Table.

Adaptor and imaging oligos

Following the strategy of Mateo et al.,¹⁶ we used adaptors to link fluorescently-labeled imaging oligos to their complementary barcode sequences in the primary Oligopaint library. Adaptors were 62 nt long, and were constructed as follows (from 5' to 3'): (1) a 20 nt region complementary to the primary oligopaints library; (2) a bridge of 10 nt; and (3) a 32 nt sequence complementary to the fluorescent imaging oligo. Adaptor sequences can be found in [Table S3](#).

We used a single 32 nt imaging oligo with a sequence complementary to all adaptors and labeled with a cleavable Alexa 647 fluorophore. At the end of each cycle, the fluorescent signal of the imaging oligo was extinguished by chemical bleaching (see image acquisition section). Instead, fiducial markers were imaged using a 32 nt imaging oligo labeled by a non-cleavable Rhodamine Red fluorophore. Fiducials were displaced and reloaded every 10 cycles using a displacement oligo (see [key resources table](#)). Adaptors and imaging oligos were synthesized by Integrated DNA Technologies (IDT; Coralville, USA). See [key resources table](#) for sequences of imaging oligos.

Embryo collection and fixation

Oregon-R w^{1118} flies were used for the WT strain. For the mutant line, the Pc^{XT109} strain was used. It consists in a null mutant⁶³ that was balanced over the KrGFP-TM3, Sb^1 balancer (TKG: obtained from BL#5195 of the Bloomington Drosophila Stock Center). Flies were maintained at room temperature with natural light/dark cycles and were grown on standard cornmeal yeast media at 21°C.

Following a pre-laying period of 16–18 H in cages with yeasted 0.4% acetic acid agar plates, agar plates were changed for new ones so flies can lay eggs during the corresponding time (1.5 H for NC14 embryos, 4 H for S15-16 embryos and mutants) on the new plates. Embryos were then incubated at 25°C for the corresponding time to obtain the desired developmental stage for fixation (1 H for NC14, 12 H for S15-16 and mutants). For fixation, embryos were dechorionated with bleach for 5 min and thoroughly rinsed with water. They were fixed in a fixation buffer (1:1 mixture of 4% methanol-free formaldehyde in PBS and heptane) by agitating vigorously for 15 s and then letting stand the vial for 25 min at RT. The bottom formaldehyde layer was replaced by 5 mL methanol and embryos were vortexed for 30 s. Embryos that sank to the bottom of the tube, devitellinized, were rinsed three times with methanol. Embryos were stored in methanol at –20°C until further use.

Hybridization of Hi-M library

Embryos were rehydrated by incubating them sequentially for 5 min at RT on a rotating wheel, using 1 mL of each of the following solutions: I) 90% methanol, 10% PBT; II) 70% methanol, 30% PBT; III) 50% methanol, 50% PBT; IV) 30% methanol, 70% PBT; V) 100% PBT. Then embryos were RNase treated during 2h at RT, and permeabilized in 0.5% Triton/PBS during 1h. Next, embryos are incubated for 20 min at RT on a rotating wheel sequentially in the following Triton/pHM solutions (pHM: 2X SSC, NaH₂PO₄ 0.1M pH = 7, 0.1% Tween 20, 50% formamide (v/v)): I) 80% PBS-Triton, 20% pHM; II) 50% PBS-Triton, 50% pHM; III) 20% PBS-Triton, 80% pHM; IV) 100% pHM. Then 225 pmol of primary probe were diluted in 25 μ L of FHB (FHB = 50% Formamide, 10% dextran sulfate, 2X SSC, Salmon Sperm DNA 0.5 mg mL). Primary probes and embryos were denatured by incubating them 15 min at 80°C. Embryos were then transferred to a 500 μ L PCR tube, next pHM was removed from embryos and 30 μ L of the denatured probes were added. Embryos were then placed into a thermocycler with the following program: Starting from 80°C, 43 cycles of 10 min, with a temperature drop of –1°C/cycle, then incubation at 37°C indefinitely. Embryos were then transferred back to a 1.5 mL tube, and sequentially washed for 20 min in the following solutions: I) 50% (v/v) formamide, 2 \times SSC; repeat this wash once; II) 40% (v/v) formamide, 2 \times SSC; III) 30% formamide, 70% PBT; IV) 20% formamide, 80% PBT; V) 10% formamide, 90% PBT; VI) 100% PBT; VII) 100% PBS-Triton. Washes I-IV were performed at 37°C in a thermal mixer with agitation (900 r.p.m.); washes V-VII were performed at RT on a rotating wheel. An additional crosslink in 4% PFA was performed. Embryos were washed and resuspended in PBS, and stored at 4°C until use.

Microscope setup

Experiments with NC14 embryos were performed on a home-made wide-field epifluorescence microscope built on a RAMM modular microscope system (Applied Scientific Instrumentation) coupled to a microfluidic device as described previously.^{22,23} Samples were imaged using a 60x Plan-Achromat water-immersion objective (NA = 1.2, Nikon, Japan). The objective lens was mounted on a closed-loop piezoelectric stage (Nano-F100, Mad City Labs Inc. - USA). Illumination was provided by 3 lasers (OBIS-405/640 nm and Sapphire-LP-561 nm, Coherent – USA). Images were acquired using a sCMOS camera (ORCA Flash 4.0V3, Hamamatsu – Japan), with a final pixel size calibrated to 106 nm. A custom-built autofocus system was used to correct for axial drift in real-time and maintain the sample in focus as previously described.²² A fluidic system was used for automated sequential hybridizations, by computer-controlling a combination of three eight-way valves (HVXM 8-5, Hamilton) and a negative pressure pump (MFCS-EZ, Fluigent) to deliver buffers and secondary readout probes onto a FCS2 flow chamber (Bioprotechs). Software-controlled microscope components, including camera, stages, lasers, pump, and valves were run using a custom-made software package written for Labview (available at [HiM acquisition Labview](https://zenodo.org/record/6379944)) or Qudi-HiM, our most recent version written in python ([qudi-HiM](https://zenodo.org/record/6379944)).⁶⁴ Qudi-HiM was archived at <https://zenodo.org/record/6379944> (<https://doi.org/10.5281/zenodo.6379944>).

Experiments with S15-S16 and Pc del embryos were performed on an AxioObserver microscope coupled to a LSM800 laser-scanning confocal detection (Zeiss, Germany). Samples were imaged using a 63x, NA = 1.2 water-immersion objective (W DICII, Zeiss). Illumination was provided by 3 laser lines (405/561/640 nm). Images were acquired with a pixel size of 100 nm, and 0.5 μ m z-slices. A pinhole size of 62 μ m was used. ZEN 2.3/6 blue edition (.NET Framework Version: 4.0.30319.42000) was used for acquisition. Focus reproducibility during the experiment was ensured by the built-in autofocus tools available in ZEN.

Sequential hybridizations were performed using a computer-controlled fluidic system. In brief, a peristaltic pump (Instech, P720) coupled to an eight-way valve (HVXM 8-5, Hamilton) delivers the buffers into a FCS2 flow chamber (Bioprotechs). Barcodes were injected sequentially using a home-made delivery platform composed of a rotating tray where the tubes are arranged (Physik Instrumente, M-404.4PD). A needle coupled to a linear stage (Physik Instrumente, VT-80) is used to inject the barcodes into the chamber. A second peristaltic pump (Instech, P720) is coupled to the needle and a two-way valve (HVXM 2-5, Hamilton), to wash the residual barcode solution from the needle between cycles. Flow rate is constantly monitored (FRP, flow-rate platform, Fluigent) in order to control the injected volumes and ensure reproducible hybridization conditions for all probes.

Finally, an XY translation stage (MS2000, Applied Scientific Instrumentation) is used to select the positions of the embryos. Pumps, valves, and translation stages were controlled using a custom-made software package developed in LabView 2015 (National

Instruments). Synchronization between injections and confocal acquisitions was ensured using a trigger box (SVB-1 Zeiss, Germany) and an analog voltage output device (USB-3104, Measurement computing).

Image acquisition

Embryos labeled with the primary library were attached to a poly-L-lysine coated coverslip, and placed into the FCS2 fluidics chamber. Fiducial mark labeling with a Rhodamine labeled readout probe and DAPI staining were performed in the chamber, using the fluidics system to inject solutions and perform washes. For image acquisition, the fluidics system harbored: 1 tube with 50 mL of washing buffer (WB, 2X SSC, 40% v/v formamide), 1 tube with 50 mL of 2x SSC, 1 tube with 20 mL of imaging buffer (IB, 1xPBS, 5% w/v glucose, 0.5 mg/mL glucose oxidase and 0.05 mg/mL catalase), 1 tube with 50 mL of chemical bleaching buffer (CB, 2X SSC, 50 mM TCEP hydrochloride), and 19 tubes with 2 mL of each readout probe solution (25 nM readout probe, 2X SSC, 40% v/v formamide). To avoid degradation by oxygen, IB was stored under a layer of mineral oil throughout the experiment, and renewed every 12 h.

Several 200 μm \times 200 μm fields of view (FOV) containing embryos were selected, using our home-made LabView software package. Z stacks of 15–20 μm were selected, with steps of 250 nm in the widefield setup and 500 nm in the Airyscan.

DAPI was imaged first, together with fiducial marks, using the 405, and the 561 nm laser lines. Barcode imaging was also performed automatically using our home-made Labview software package, which controlled the fluidics system and the XY translations stage and synchronized image acquisition performed by ZEN. Briefly, the chamber was filled with 1.7 mL barcode probe solution over \sim 17 min to ensure binding of readout probes. Next, the sample was washed with 1.5 mL of wash buffer for 10 min. Then 1.5 mL of 2X SSC were flushed during 10 min and finally 1.2 mL of imaging buffer was injected in \sim 12 min. Flow was stopped, and the FOVs were imaged in two channels by exciting at 561 and 641 nm to image fiducial marks and barcode probes, respectively. After imaging, the fluorescence signal of the barcode probes was cleaved using chemical bleaching by flowing 1.5 mL of CB buffer for 10 min. The Rhodamine-labeled fiducial barcode was insensitive to chemical removal. After chemical bleaching, the chamber was flushed with 1.5 mL of 2X SSC for 10 min and a new hybridization cycle started. All buffers were freshly prepared and filtered for each experiment. Barcodes displayed a labeling efficiency in the 40–65% range (Figure S2C). Images were acquired using our home-made Labview software package or using qudi-HiM, a python-based software package developed for the acquisition of Hi-M datasets⁶⁴ (see [data and code availability](#) sections).

Polymer modeling

A block copolymer of $N = 866$ beads, each of size $a = 20\text{kb}$, matching the genomic size and distribution of the experimental probes was implemented and simulated by Monte Carlo simulations⁶⁵ on a Face-Centered Cubic lattice (FCC). This lattice polymer model has proven to be extremely precise up to second order corrections when compared to analytical results for DNA hybridization/melting⁶⁶ and for the unwinding dynamics.⁶⁷ Beads were divided into two classes in all simulations: Pc beads, that displayed a finite interaction strength U ; and non-Pc beads, for which $U = 0$. To study the behavior of a block copolymer, we used two estimators. The first estimator is the internal energy E defined as:

$$E = -\frac{U}{N} \sum_{\langle i,j \rangle} \varphi_i \varphi_j,$$

where U is the interaction energy between two Pc beads, φ_i is the occupation variable of the vertex i of the lattice by a Pc bead (1 if a Pc bead is present and 0 otherwise) and the sum $\sum_{\langle i,j \rangle}$ runs over all the pairs $\langle i,j \rangle$ of nearest-neighbor Pc beads on the lattice. By

construction, the internal energy estimates the averaged number of Pc-Pc interactions, which increases from the coil to the globule regime as U increases. The second estimator is the squared radius of gyration defined as:

$$R_g^2 = \frac{1}{N} \sum_i (\vec{R}_i - \vec{R}_{cm})^2,$$

where \vec{R}_i is the position vector of the monomer i and $\vec{R}_{cm} = \frac{1}{N} \sum_i \vec{R}_i$ is the center of mass of the polymer. R_g^2 characterizes the spatial extension of the polymer, which displays a large drop from the coil to the globule regime as U increases. This change of the spatial conformation is the cause of the different contact probability described in Figure 1G.

In order to assess the behavior of this polymer versus U , we built the phase diagram in Figures S2H and S2I (main graph) where the internal energy E and the squared radius of gyration R_g^2 are plotted versus U . To do so, R_g^2 was sampled from $U = 0$ over $2 \cdot 10^5$ configurations. N^2 Monte Carlo steps were performed to decorrelate the polymer between two samplings. Subsequently to the completion of the sampling at a given U , the value of U was increased by $0.05k_B T$, the system was thermalized during 10^7 Monte Carlo steps and the sampling procedure was resumed at this new interaction energy. In the inset, we plotted the fluctuations of both E and R_g^2 that were calculated in the same manner. Different values of U were used, to match experimental data: for all observables presented in the main text (Frequency versus genomic distance; histogram of pairwise interactions and proximity map between *Ubx*, *abd-A* and *Abd-B*) we used $U = 0.8 k_B T$ for early embryos and $U = 0.9 k_B T$ for late embryos.

QUANTIFICATION AND STATISTICAL ANALYSIS

Data analysis

Airyscan images (.czi format) were converted to TIFF files using the Bio-Formats plugin in Fiji (Schneider, Rasband, and Eliceiri⁶⁸; Schindelin et al.,⁶⁹ <https://github.com/ome/bioformats>.⁷⁰ Raw images were deconvolved using Huygens Professional version 20.04 (Scientific Volume Imaging, the Netherlands, <https://svi.nl/>), via the CMLE algorithm (SNR:20, 40 iterations).

The following analysis steps were performed with home-made scripts written in MATLAB 2019b (The MathWorks, Inc., Natick, United States) and available from [HiM analysis MATLAB](#), or our most recent version written in python (pyHiM), available from <https://github.com/marcnol/pyHiM> and archived at: <https://osf.io/updfw> (<https://doi.org/10.17605/OSF.IO/UPDFW>).⁷¹ Indications for how to download this code are provided in the “Data and code availability section” below. First, X-Y drift is corrected for each hybridization cycle. A global X-Y correction for each cycle is obtained by cross-correlating the images of the fiducial of each cycle to that of the reference fiducial (reference cycle). This produces a single 3D vector for each barcode cycle that represents a *global* correction applied to the whole FOV. Second, an adaptive thresholding is used to pre-segment the spots of each fiducial for all FOVs and for all barcode cycles. The 3D coordinates of each fiducial spot in each FOV and cycle were then estimated by segmentation and 3D Gaussian fitting. Fiducial spots with sizes larger than the diffraction limit (~2.2 pixels in our microscope) were filtered out. Third, we obtained ‘local’ 3D correction vectors for each cell in each FOV by first using the global X-Y correction vector to pre-align fiducial spots in each cycle to fiducial spots in the reference cycle. Then, image-based cross-correlation of these pre-aligned fiducial spots were used to reach sub-pixel accuracy in the correction vector. This approach allowed for 3D, subpixel accuracy drift-correction across the whole FOV (Figure S2D). Fourth, barcode spots were segmented for all hybridization cycles in batch processing mode using optimized adaptive thresholding. The 3D coordinates of each barcode were then determined by 3D Gaussian fitting of the segmented regions. These positions were corrected for drift by using the closest fiducial barcode vector obtained from the previous analysis step. Nuclei were segmented from DAPI images by adaptive local thresholding and watershed filtering. Then, tracing was performed by attributing the unique set of 3D corrected barcode localizations falling within each DAPI mask. No correction for repeated barcodes was applied. Single nuclei PWD matrices were obtained by calculating the pairwise distances between barcode coordinates belonging to the same trace. Segment-specific PWD maps were obtained by grouping together the traces located within each segment, manually identified from projected DAPI images.

In Figures 1C–1E, the proximity frequency was obtained as the number of nuclei where the pairwise distances were lower or equal to 250 nm, normalized by the number of nuclei containing both barcodes. Pairwise distance maps were calculated by the median of the distribution for each barcode combination.

In Figures 2A and 2B, for each Pc anchor we calculated the frequency of cells co-localizing with at least one Pc target. Bootstrap-ping was used to calculate distributions.

In Figure S2G, we calculated the observed/expected proximity map by plotting the dependence of proximity frequency to genomic distance and fitting it with a power law. The observed/expected proximity map was obtained by normalizing the observed proximity by the expected proximity map derived from the power law fit.